Supplementary Information

High-efficiency ammonia electrosynthesis from nitrate on ruthenium-induced trivalent cobalt sites

Longcheng Zhang,[a,b] Yuan Liu,[b] Ling Li,[c] Tianze Wu,[b] Qian Wu,[b] Justin Zhu Yeow Seow,[b] Xiu Lin,[b] Shirong Sun,[b] Leonhard Tannesia,[b] Kai Tang,[b] Dongsheng Shao,[b] Shibo Xi,[d] Xiaodong Guo*[a] and Zhichuan J. Xu*[b,e]

[a] School of Chemical Engineering, Sichuan University, Chengdu 610065, China

[b] School of Material Science and Engineering, Nanyang Technological University, Singapore 639798, Singapore

[c] Analytical & Testing Centre, Sichuan University, Chengdu 610064, China

[d] Institute of Sustainability for Chemicals, Energy and Environment (ISCE^2), Agency for Science, Technology and Research (A*STAR), Singapore 627833, Singapore

[e] Centre for Advanced Catalysis Science and Technology, Nanyang Technological University, Singapore 639798, Singapore

* Corresponding author email: xuzc@ntu.edu.sg; xiaodong2009@scu.edu.cn

Experiment Section

Synthesis of $Co(OH)_2$/CC: First, a well-cut small piece of CC (2 × 3 cm^2) was soaked in concentrated nitric acid at 80 ºC for 2 h, then sonicated in acetone and deionized water (15 min each), and subsequently dried in an oven at 70 ºC for 1 h. $Co(OH)_2$ nanosheets were electrodeposited on CC using a Metrohm Autolab workstation in a three-electrode setup, where CC, Pt foil, and saturated calomel electrode as the working, counter, and reference electrodes, respectively. Electrodeposition was conducted in a 50 mL solution containing 50 mM $Co(NO_3)_2 \cdot 6H_2O$ at an applied potential of −1 V for 900 s. Afterward, the electrode was rinsed with deionized water and dried at 70 °C.

Synthesis of Ru-$Co(OH)_2$/CC: A piece of $Co(OH)_2$/CC (2 × 3 cm^2) was immersed in 20 mL of 5 mM $RuCl_3$ solution for 20 min. The resulting material was thoroughly rinsed with deionized water before being dried at 70 ºC overnight.

Materials characterizations: The crystal structure of the samples was analyzed using XRD on a Bruker D2 Phaser. Sample morphology was examined by SEM using a JEOL JSM-7600F microscope. TEM, HRTEM, and the related elemental mapping were conducted using a JEOL JEM-2100 Plus microscope. The electronic states of materials were examined by XPS using a Shimadzu Kratos Axis Supra instrument. UV-Vis absorbance spectra were acquired with a Shimadzu UV-2700 spectrophotometer. ^1H NMR signals for isotope-labeling experiments were recorded on a Bruker 400 MHz system. XAS, including XANES and EXAFS, was conducted at the XAFCA beamline at the Singapore Synchrotron Light Source. Data processing was conducted using the ATHENA module in the Demeter software suite.

Electrochemical measurements: Prior to testing, the Nafion 117 membrane (3 × 3 cm^2, 183 μm thick) was protonated vis sequential treatments: (i) immersion in 5% H_2O_2 at 80 °C for 2 h, (ii) treatment in 0.5 M H_2SO_4 at 80 °C for 2 h, and (iii) boiling in deionized water for 1 h. The cathode and anode compartments were each filled with 50 mL of 1 M KOH solution containing 2,000 ppm NO_3^- at room temperature unless otherwise specified. Before each measurement, high-purity Ar gas (99.99%) was bubbled into both compartments of the H-cell for at least 30 min. EIS was carried out to determine solution resistance, and all potentials were corrected with 50% iR compensation unless otherwise noted. Chronoamperometry was conducted at constant applied potentials for 30 min, with stirring at 900 revolutions per minute, to monitor current density over time. All potentials were converted to the RHE scale: $E_{RHE} = E_{Hg/HgO} + 0.0591 \times pH + 0.098$ V. NO_3^- removal tests were evaluated in a batch H-cell containing 1 M KOH with 2,000 ppm NO_3^- over 70 min, with electrolyte samples collected every 10 min for product quantification.

Calculation of EE: EE is calculated with the following equation:

$$EE = (1.23 - E_{NH_3}) \times FE_{NH_3} / (1.23 - E)$$

Here, E_{NH3} (0.69 V) is the equilibrium potential for NO_3^- electroreduction to NH_3,[1] FE_{NH3} is the FE for NH_3, 1.23 V represents the equilibrium potential of water oxidation (assuming zero overpotential), and E is the potential vs. RHE after 80% iR compensation.[2]

In situ Raman spectroscopy: In situ Raman measurements were carried out by confocal Raman spectroscopy (Horiba Jobin Yvon Co., France) equipped with a 633 nm laser. All the Raman measurements were performed with a 50× microscope objective. Raman spectra were recorded systematically at various potentials using a Metrohm Autolab workstation. The quartz electrochemical cell was placed beneath the objective lens.

^{15}N isotope-labelling experiment: To qualitatively confirm the source of NH_3, 1 M KOH containing 2,000 ppm $K^{15}NO_3$ (>98 atom%^{15}N) was used as the feeding electrolyte. Specifically, after $^{15}NO_3^-$ electroreduction for 30 min, the electrolyte was collected, diluted to the appropriate detection range, and adjusted to pH 2 using 0.1 M HCl. Subsequently, 0.5 mL of this prepared solution was mixed with DMSO-d_6 (hexadeuterodimethyl sulfoxide) containing 0.04 wt% maleic acid for ^{1}H NMR measurements.

Quasi in situ EPR tests: EPR measurements were conducted to detect radicals or intermediates generated during electrochemical reactions. Chronoamperometry was performed at a constant potential for 5 min, during which radicals or intermediates generated were trapped by DMPO. The solution was then immediately extracted for subsequent EPR analysis.

Computational details: All calculations in this work were carried out using the Vienna Ab Initio Simulation Package. The valence electron states were represented using a plane-wave basis set with an energy cutoff of 500 eV, while the projector-augmented wave method was applied to account for core electrons. Convergence in the electronic self-consistency loop was ensured with a threshold of 10^{-5} eV. For structural relaxations, all atomic coordinates and lattice parameters were optimized until residual forces were reduced below 0.01 eV/Å. A Gaussian smearing method with a width of 0.05 eV was adopted for integration. For structural optimizations, A Γ centered Monkhorst-Pack k-point grid of 3 × 3 × 1 was utilized during structural optimizations, which was refined to 6 × 6 × 1 for DOS calculations. To eliminate interactions between periodic images, a vacuum layer of 15 was introduced. While the van der Waals (vdW) forces were excluded due to the robust interfacial bonding, the dispersion-corrected DFT-D3 method was applied to describe vdW interactions where relevant. Bader charge analysis was performed with tools developed by Henkelman et al.[3]

NO_3^- Electrolysis in MEA System: The custom-built MEA setup with a serpentine flow channel included two titanium current collector plates (cathode and anode), two polytetrafluoroethylene gaskets each featuring a 4 cm^2 window, and an Alkymer W-25 anion exchange membrane in between. An IrO_2/C ink, sprayed onto PTF, acted as the anode. The cell was compressed by applying 6 N•m of torque to each of the four bolts. A solution of 1 M KOH containing 2,000 ppm NO_3^- was circulated from the electrolyte reservoir through the cathode side, while another 1 M KOH solution was circulated on the anode side. A fully sealed circulation system was used to prevent NH_3 volatilization. To convert the produced NH_3 into NH_4Cl, the reaction electrolyte was transferred to a sealed bottle connected to another containing an HCl solution (0.3 M, 200 mL). Inert Ar gas (100 sccm) was supplied for 12 h, enabling selective NH_3 extraction through air stripping and trapping in the HCl solution to form NH_4Cl. Water was removed from the product using a rotary evaporator, yielding NH_4Cl as a white powder. Residual moisture was removed in a box oven, ensuring complete conversion of NO_3^- to NH_4Cl powder.

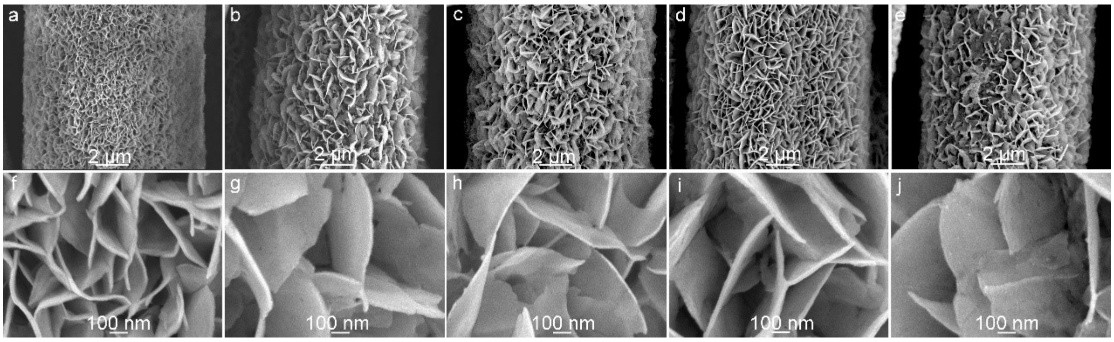

Fig. S1. Low- and high-magnification SEM images of (a, f) $Co(OH)_2$/CC, (b, g) Ru-0.2-$Co(OH)_2$/CC, (c, h) Ru-1-$Co(OH)_2$/CC, (d, i) Ru-5-$Co(OH)_2$/CC, and (e, j) Ru-10-$Co(OH)_2$/CC.

SEM images in Figs. S1a-j show that the surfaces of nanosheets become progressively rougher with an increase in $RuCl_3$ solution concentrations from 0.2 to 5 mM. However, when the concentration of $RuCl_3$ solution was further increased to 10 mM, the original vertical nanosheets slightly collapsed and adhered to one another (Fig. S1j)

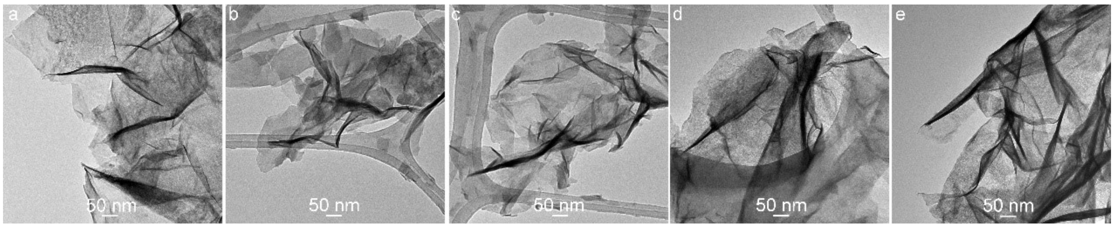

Fig. S2. TEM images of (a) $Co(OH)_2$, (b) Ru-0.2-$Co(OH)_2$, (c) Ru-1-$Co(OH)_2$, (d) Ru-5-$Co(OH)_2$, and (e) Ru-10-$Co(OH)_2$.

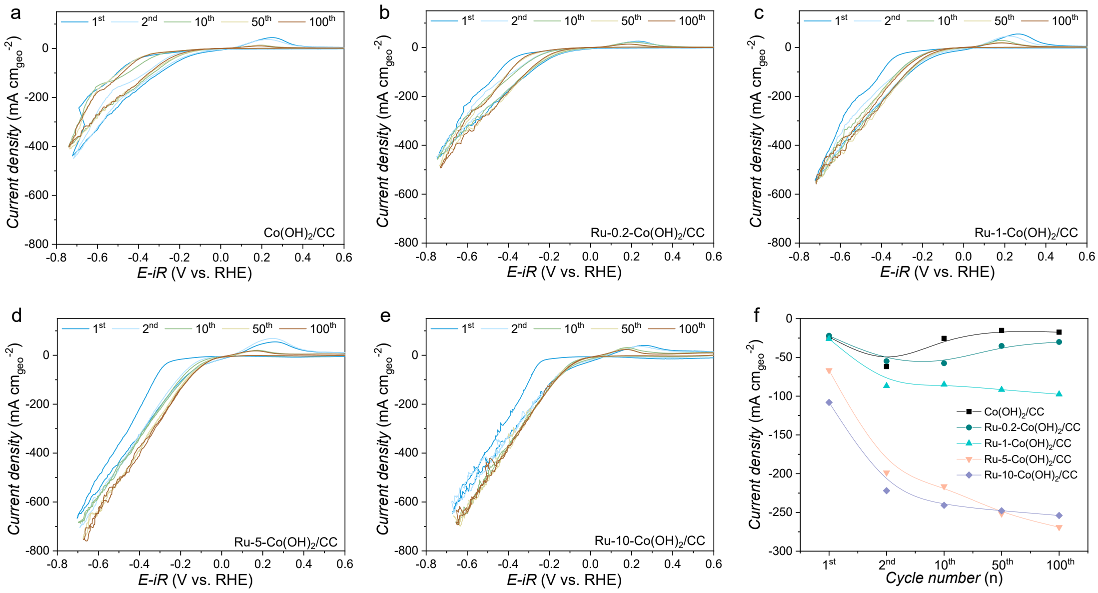

Fig. S3. CV curves for (a) Co(OH)$_2$/CC, (b) Ru-0.2-Co(OH)$_2$/CC, (c) Ru-1-Co(OH)$_2$/CC, (d) Ru-5-Co(OH)$_2$/CC, and (e) Ru-10-Co(OH)$_2$/CC from the 1st to the 100th cycle in Ar-saturated 1 M KOH solution with 2,000 ppm NO_3^-. (f) Evolution of the current density at –0.3 V vs. RHE during cycling for Co(OH)$_2$/CC and Ru-x-Co(OH)$_2$/CC.

As shown in Fig. S3a, the Co(OH)$_2$/CC exhibits a decline in current density after the initial cycles, indicating deactivation. This can be attributed to the intrinsic instability of pristine Co(OH)$_2$ under the applied electrochemical conditions. In contrast, the Ru-doped Co(OH)$_2$/CC electrodes show a continuous increase in current density with cycling, which we attribute to the progressive reconstruction of the active surface. The presence of Ru promotes the formation of more active catalytic sites during electrochemical cycling.

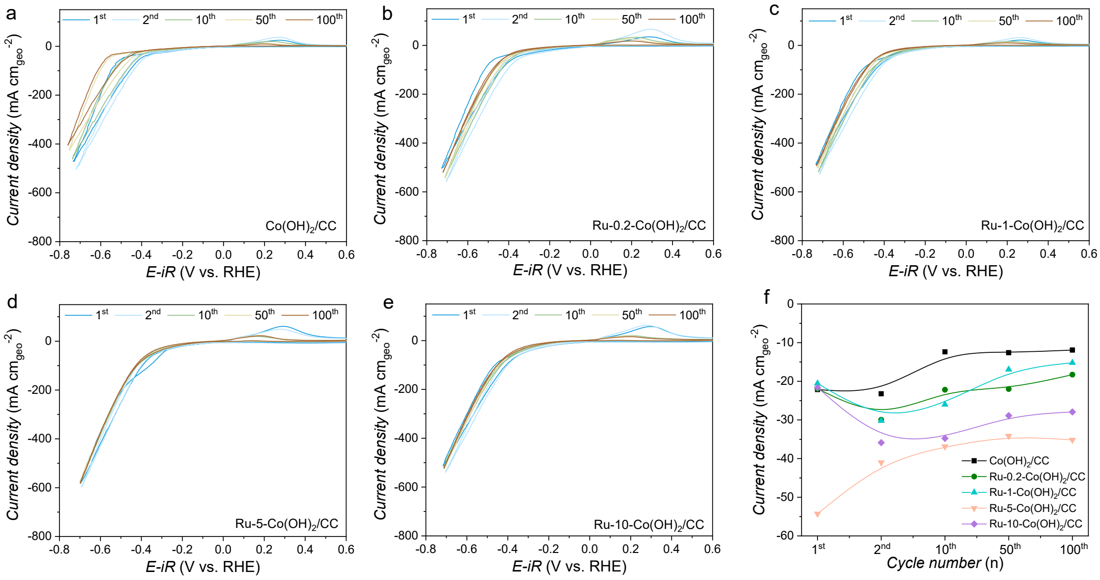

Fig. S4. CV curves for (a) Co(OH)$_2$/CC, (b) Ru-0.2-Co(OH)$_2$/CC, (c) Ru-1-Co(OH)$_2$/CC, (d) Ru-5-Co(OH)$_2$/CC, and (e) Ru-10-Co(OH)$_2$/CC from the 1st to the 100th cycle in Ar-saturated 1 M KOH solution. (f) Evolution of the current density at –0.3 V vs. RHE during cycling for Co(OH)$_2$/CC and Ru-x-Co(OH)$_2$/CC.

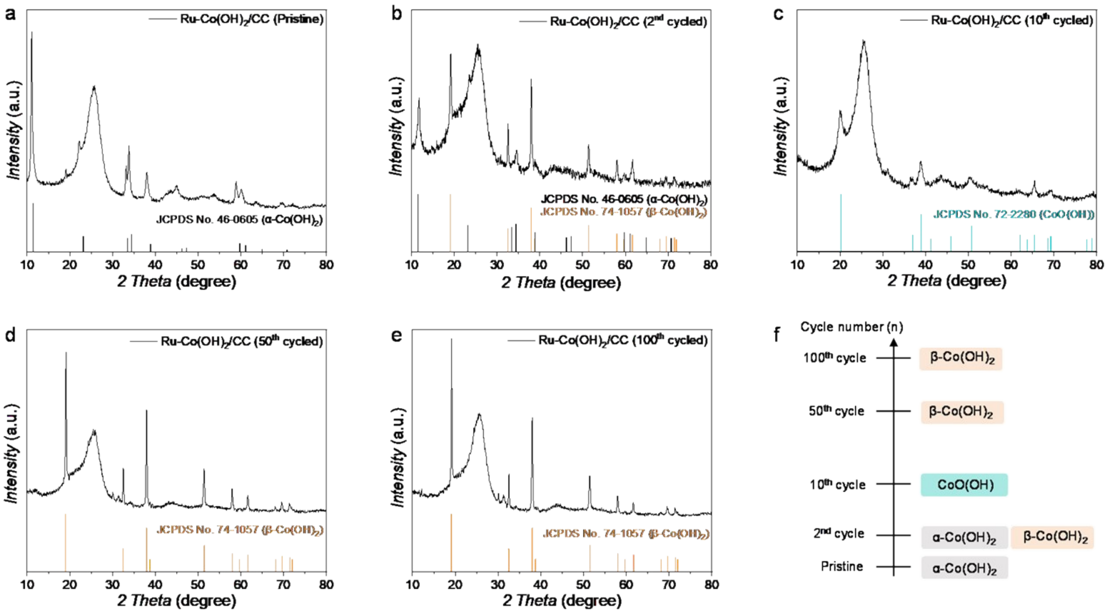

Fig. S5. XRD patterns of (a) pristine Ru-Co(OH)$_2$/CC, (b) 2nd cycled Ru-Co(OH)$_2$/CC, (c) 10th cycled Ru-Co(OH)$_2$/CC, (d) 50th cycled Ru-Co(OH)$_2$/CC, and (e) 100th cycled Ru-Co(OH)$_2$/CC in Ar-saturated 1 M KOH solution with 2,000 ppm NO_3^-. (f) Phase transition of Ru-Co(OH)$_2$/CC from pristine to 100th CV cycle in Ar-saturated 1 M KOH solution with 2,000 ppm NO_3^-.

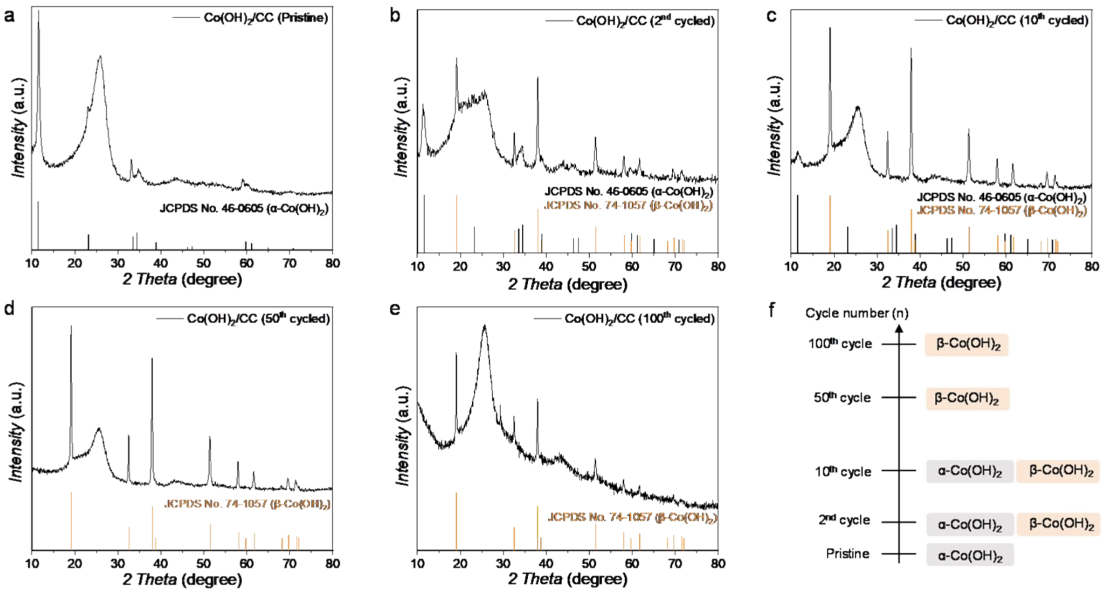

Fig. S6. XRD patterns of (a) pristine $Co(OH)_2$/CC, (b) 2nd cycled $Co(OH)_2$/CC, (c) 10th cycled $Co(OH)_2$/CC, (d) 50th cycled $Co(OH)_2$/CC, and (e) 100th cycled $Co(OH)_2$/CC in Ar-saturated 1 M KOH solution with 2,000 ppm NO_3^-. (f) Phase transition of $Co(OH)_2$/CC from pristine to 100th CV cycle in Ar-saturated 1 M KOH solution with 2,000 ppm NO_3^-.

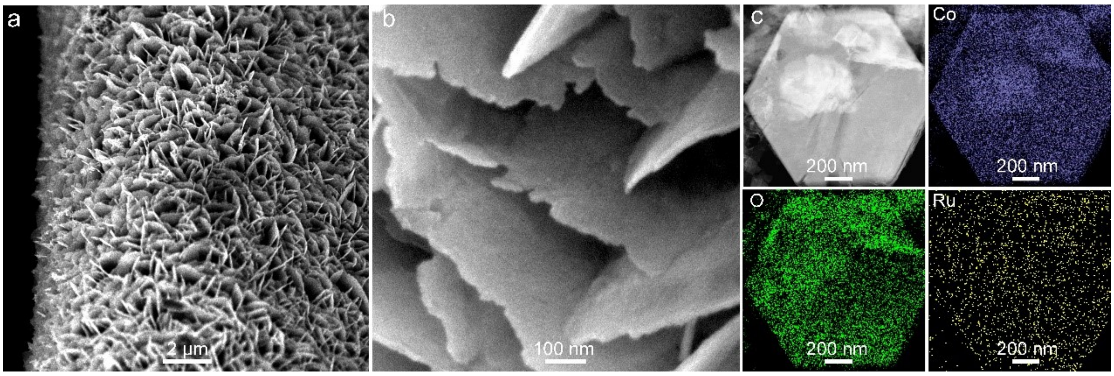

Fig. S7. (a) Low-, (b) high-magnification SEM images and (c) TEM and the related elemental mapping images of 10th cycled Ru-5-$Co(OH)_2$/CC in Ar-saturated 1 M KOH solution with 2,000 ppm NO_3^-.

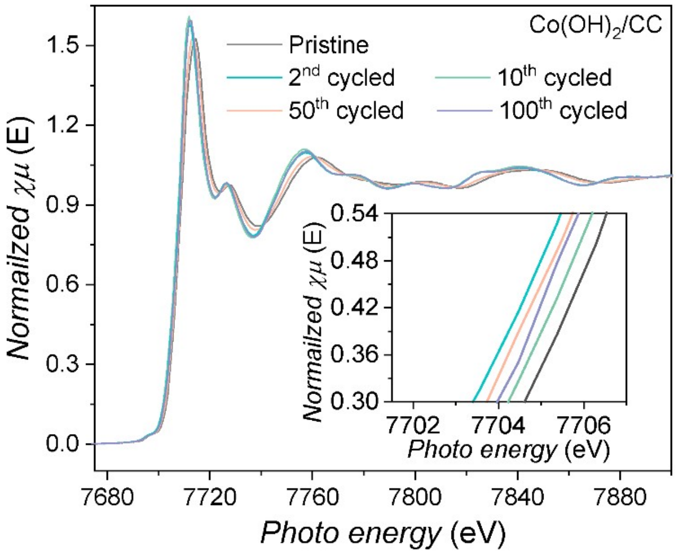

Fig. S8. Normalized Co K-edge XANES spectra of the Co(OH)$_2$/CC before and after CV cycle in Ar-saturated 1 M KOH solution with 2,000 ppm NO_3^-.

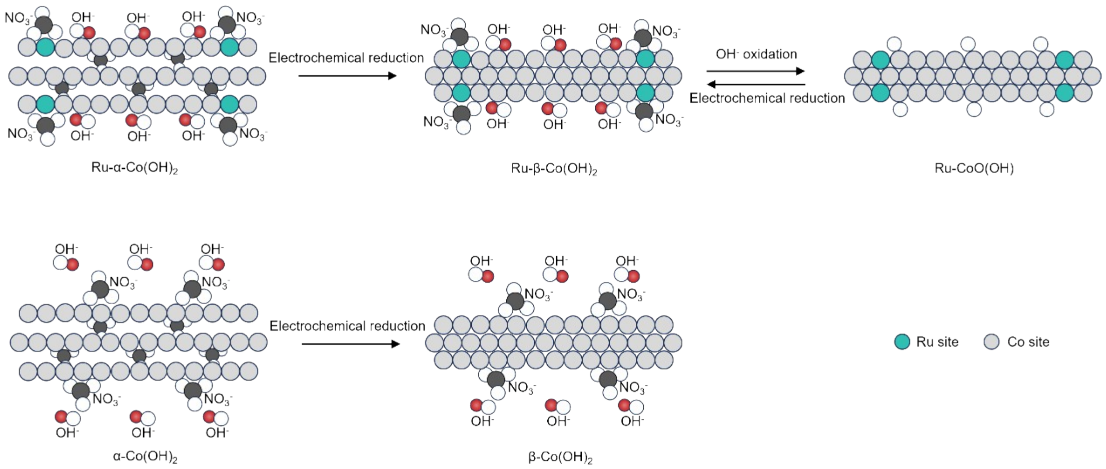

Fig. S9. Schematic illustration of the phase translation for Ru-$Co(OH)_2$ and $Co(OH)_2$ during NO_3RR.

Generally, $Co(OH)_2$ with a sheet-like structure has α- and β-phases.[4] α-$Co(OH)_2$ has an interlayer spacing of ~7.0 Å and is intercalated with anions such as chloride, carbonate, or nitrate between the adjacent positively charged layers of $Co(OH)_2$. In contrast, β-$Co(OH)_2$ has a lower interlayer spacing of ~4.6 Å without any species between the adjacent layers.[5] Ru doping enhances the OH^- adsorption capacity of $Co(OH)_2$, thereby facilitating its transition to CoO(OH) ($Co(OH)_2 + OH^- \rightarrow CoO(OH) + H_2O + e^-$). A plausible mechanism of the formation of CoO(OH) from layered $Co(OH)_2$ in Ru-$Co(OH)_2$/CC after the 10th CV cycle is the oxidation reaction with hydroxide ions.[6-8]

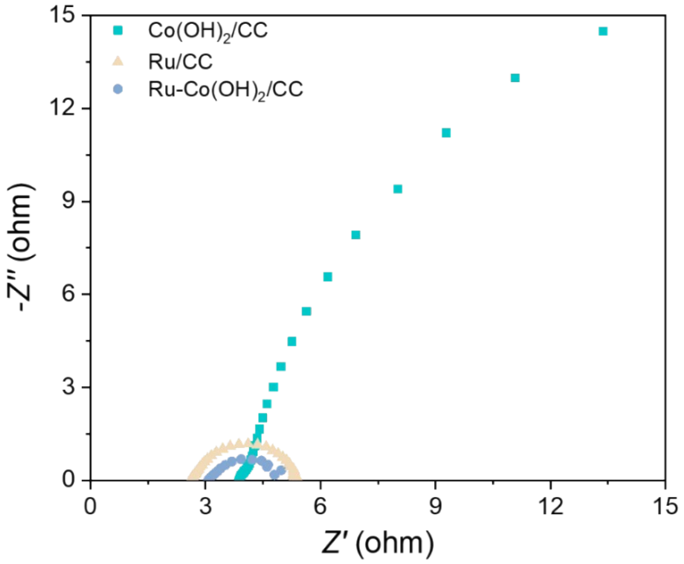

Fig. S10. Electrochemical impedance spectra of $Co(OH)_2$/CC, Ru-$Co(OH)_2$/CC, and Ru/CC at a potential of –1.1 V vs HgO/HgO in Ar-saturated 1 M KOH solution with 2,000 ppm NO_3^-.

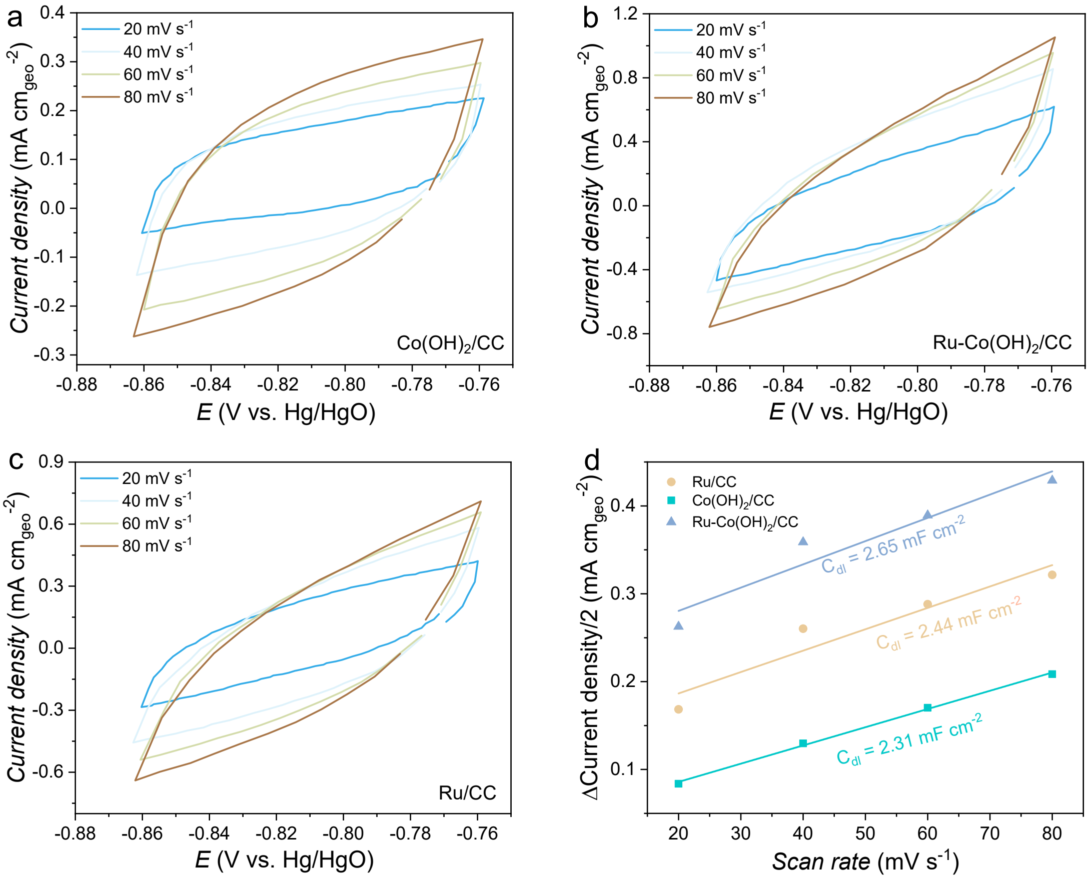

Fig. S11. CV curves of (a) $Co(OH)_2$/CC, (b) Ru-$Co(OH)_2$/CC, and (c) Ru/CC collected at the scan rates of 20, 40, 60, and 80 mV s^{-1} in Ar-saturated 1 M KOH solution. (d) Capacitance current density at –0.81 V vs. Hg/HgO as a function of scan rate for $Co(OH)_2$/CC, Ru-$Co(OH)_2$/CC, and Ru-/CC in Ar-saturated 1 M KOH solution.

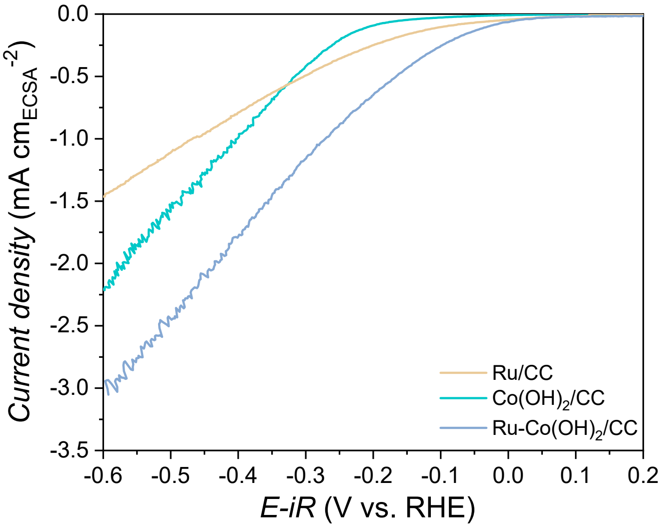

Fig. S12. ECSA-normalized LSV curves of Ru-Co(OH)$_2$/CC, Co(OH)$_2$/CC, and Ru/CC in Ar-saturated 1 M KOH solution with 2,000 ppm NO_3^-.

The double-layer capacitance values (C_{dl}) were measured by cyclic voltammetry curves at the non-Faradaic potential range. The scan rates varied from 20, 40, 60 to 80 mV s^{-1}. By plotting half of the difference in double-layer charging current densities against the scan rates, a linear relationship was obtained. The slope is the C_{dl}. The ECSA was calculated from the double-layer capacitance according to the equation below:

$$ECSA=C_{dl}/C_s$$

Where C_s is the specific capacitance, C_s is 40 μF cm^{-2} in 1 M KOH.[9]

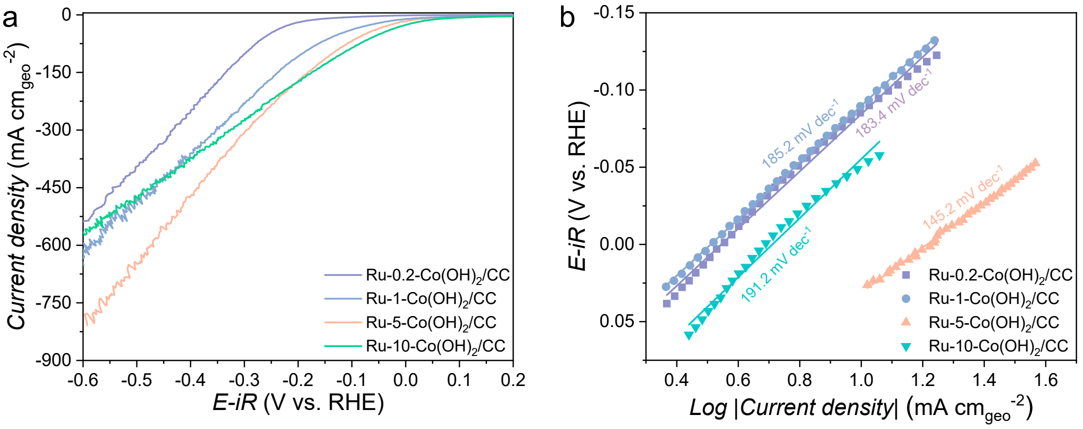

Fig. S13. (a) LSV curves and (b) Tafel plots of $Co(OH)_2$/CC, Ru-0.2-$Co(OH)_2$/CC, Ru-1-$Co(OH)_2$/CC, Ru-5-$Co(OH)_2$/CC, and Ru-10-$Co(OH)_2$/CC in Ar-saturated 1 M KOH solution with 2,000 ppm NO_3^-.

The enhanced NO_3RR activity of Ru-5-$Co(OH)_2$/CC is also evidenced by the low Tafel slope, as shown in Supplementary Fig. 13b. The Tafel slope of Ru-5-$Co(OH)_2$/CC is 145.2 mV dec^{-1}, which is lower than those of Ru-0.2-$Co(OH)_2$/CC (185.2 mV dec^{-1}), Ru-1-$Co(OH)_2$/CC (183.4 mV dec^{-1}), and Ru-10-$Co(OH)_2$/CC (191.2 mV dec^{-1}).

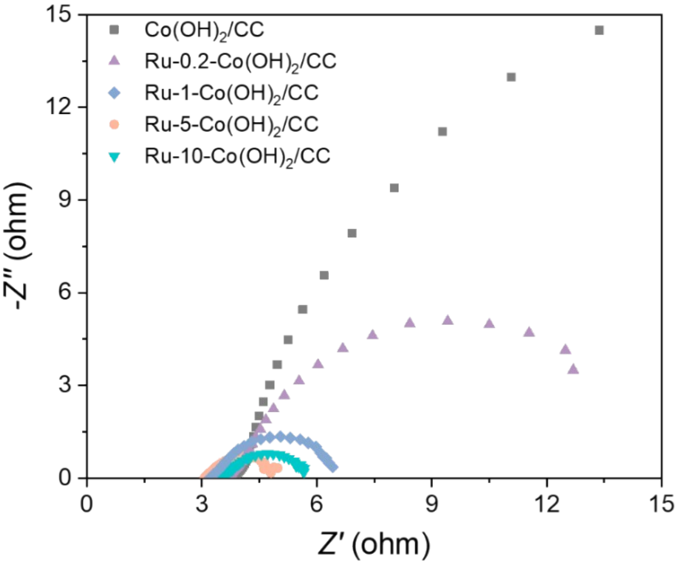

Fig. S14. Electrochemical impedance spectra of $Co(OH)_2$/CC, Ru-0.2-$Co(OH)_2$/CC, Ru-1-$Co(OH)_2$/CC, Ru-5-$Co(OH)_2$/CC, and Ru-10-$Co(OH)_2$/CC at a potential of –1.1 V vs HgO/HgO in Ar-saturated 1 M KOH solution with 2,000 ppm NO_3^-.

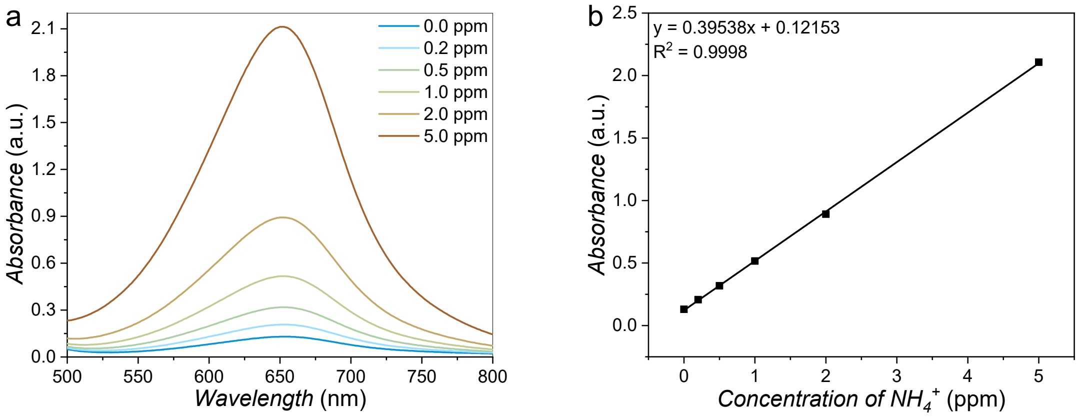

Fig. S15. (a) UV-Vis absorption spectra of indophenol assays with NH_4^+ after incubated for 2 h at room temperature. (b) Calibration curve used for estimation of NH_4^+ concentrations.

The concentration of NH_4^+ in the catholyte after electrolysis was quantified using the indophenol blue method.[10] Details of the quantitative experiment are as follows:

(1) First, 2 mL of the diluted catholyte was added to 2 mL of a 1 M NaOH coloring solution containing 5 wt% salicylic acid and 5 wt% sodium citrate.

(2) Then, 1 mL of 0.05 M NaClO oxidizing solution and 0.2 mL of 1 wt% $Na_2Fe(CN)_5NO\cdot 2H_2O$ catalyst solution were added to the above mixture.

(3) After standing for 2 h in dark conditions, the absorbance at 655 nm was measured using UV-Vis spectroscopy. The fitting curve ($y = 0.39538x + 0.12153$, $R^2 = 0.9998$) shows good linear relationship between absorbance value and NH_4^+ concentration.

Calculation of yield rate and FE

FE is calculated according to the following equations:

$$FE_{NH_3} = \frac{8 \times F \times C_{NH_3} \times V \times 10^{-6}}{17 \times Q} \times 100\%$$

Here, F is the Faradic constant (96485 C mol^{-1}), C_{NH3} is the concentrations of NH_3, V is the electrolyte volume in the cathode compartment (50 mL), Q is the total charge passed, and 17 is the molar masses of NH_3.

The NH_3 yield rate is determined as follows:

$$NH_3\,yield\,rate = (C \times V)/(17 \times t \times A)$$

Here, t is the electrolysis time and A is the electrode area (0.5 × 0.5 cm^2).

The partial current density for NH_3 is given by:

$$i_{NH_3} = i \times FE_{NH_3}.$$

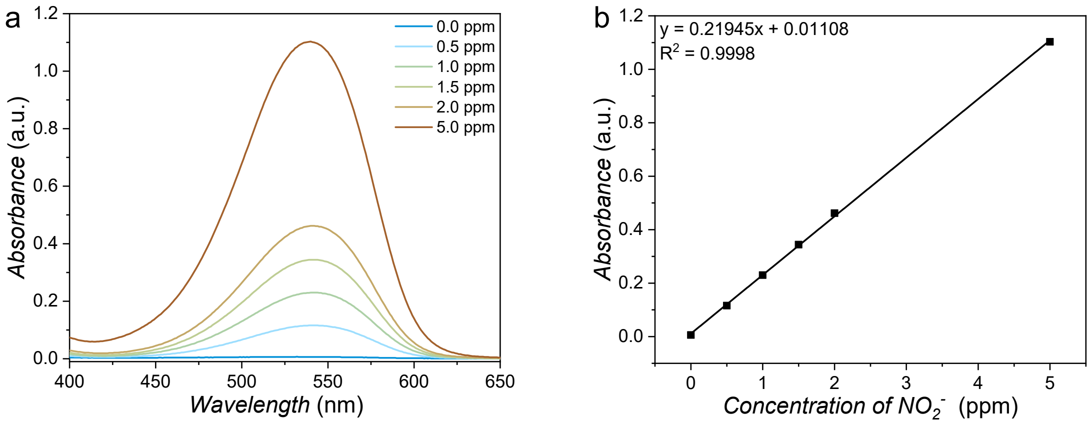

Fig. S16. The concentration-absorbance UV-Vis calibration curve of NO_2^- using different concentration of KNO_2 solutions as standards. (a) UV-Vis absorption spectra of various NO_2^- concentrations. (b) Calibration curve used for quantification of NO_2^- concentrations.

The concentration of NO_2^- in the catholyte after electrolysis was quantified using the Griess method.[11] Details of the quantitative experiment are as follows:

(1) First, a mixture of N-(1-naphthyl)-ethylenediamine dihydrochloride (0.1 g), sulfonamide (1.0 g), H_3PO_4 (2.94 mL), and deionized water (50 mL) was prepared to serve as a color reagent.

(2) Then, catholyte after electrolysis was diluted tenfold (1.0 mL) and mixed with 1.0 mL of color reagent and 2.0 mL of H_2O.

(3) After standing for 10 min, the absorbance at 540 nm was measured using UV-Vis spectroscopy. The NO_2^- concentration was quantified by using standard NO_2^- solutions ($y = 0.21945x + 0.01108$, $R^2 = 0.9998$).

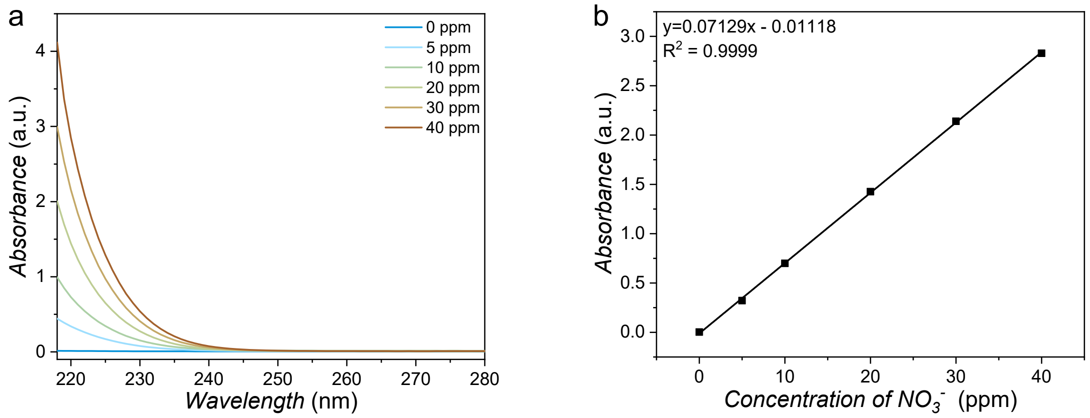

Fig. S17. The concentration-absorbance UV-Vis calibration curve of NO_3^- using different concentration of KNO_3 solutions as standards. (a) UV-Vis absorption spectra of various NO_3^- concentrations. (b) Calibration curve used for quantification of NO_3^- concentrations.

The concentration of NO_3^- in the catholyte after electrolysis was quantified using UV-Vis spectrophotometry according to the standard method.[12] Details of the quantitative experiment are as follows:

(1) First, a certain amount of electrolyte was taken out from the cathodic reaction cell and diluted to 2 mL to the detection range.

(2) Then, 40 µL of 1 M HCl with 4.0 µL of 0.8wt% sulfamic acid solution was added and mixed with 2 mL of the diluted electrolyte, then allowed to stand for 20 min under ambient conditions.

(3) The absorption spectrum was measured using a UV-Vis spectrophotometer and the absorption intensities at a wavelength of 220 nm and 275 nm were recorded. The final absorbance value was calculated by this equation: $A = A_{220\ nm} - 2A_{275\ nm}$. The concentration-absorbance curve was calibrated using a series of standard KNO_3 solutions and the KNO_3 crystal was dried at 110 ºC for 2 h in advance. The NO_3^- concentration was quantified using standard NO_3^- solutions ($y = 0.07129x - 0.01118$, $R^2 = 0.9999$).

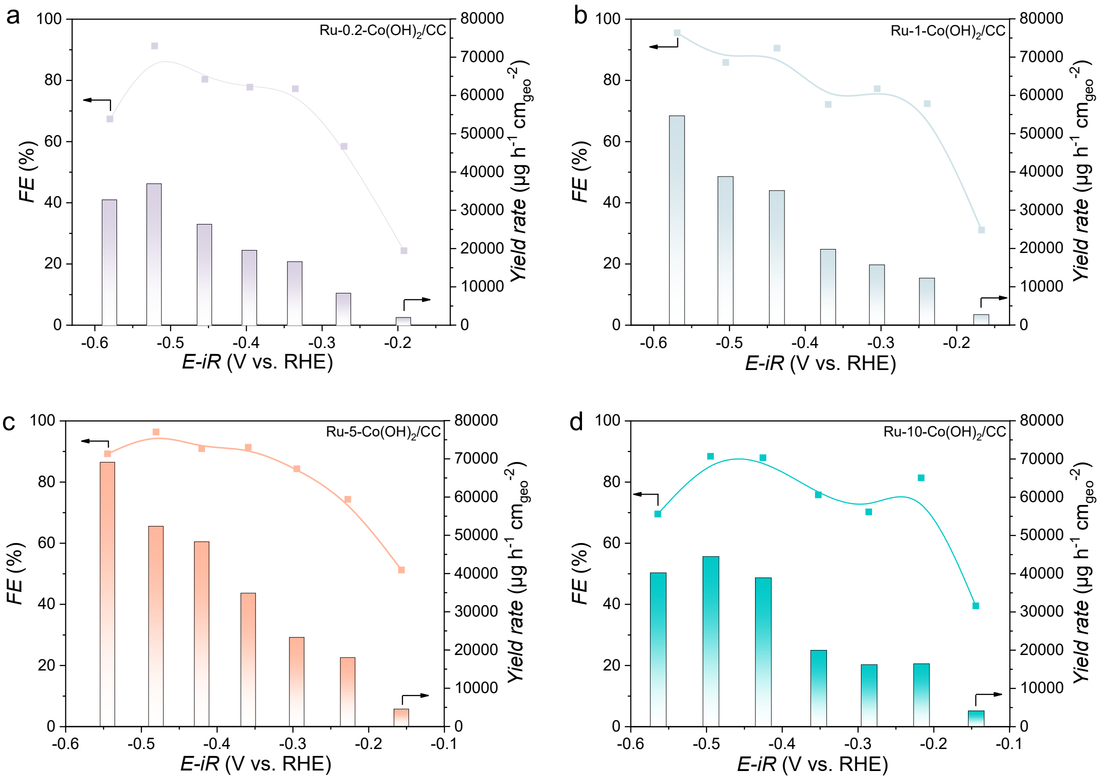

Fig. S18. NH_3 yield rates and FEs of (a) Ru-0.2-$Co(OH)_2$/CC, (b) Ru-1-$Co(OH)_2$/CC, (c) Ru-5-$Co(OH)_2$/CC, and (d) Ru-10-$Co(OH)_2$/CC in 1 M KOH solution with 2,000 ppm NO_3^-.

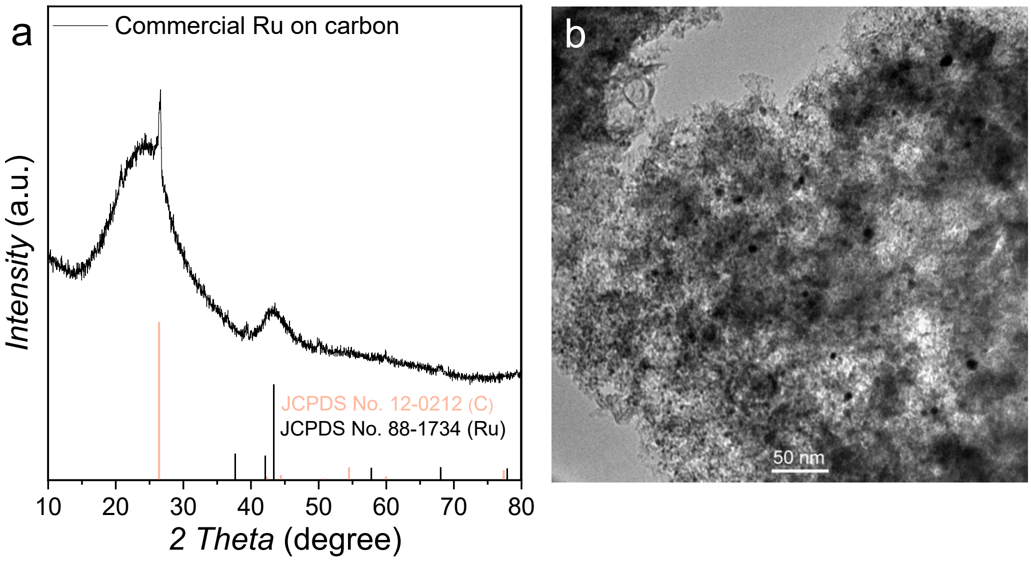

Fig. S19. (a) XRD pattern and (b) TEM image of commercial Ru on carbon.

For Ru/CC, a commercial Ru/C catalyst (5 mg) was dispersed in 1 mL of a solvent mixture (5 wt% Nafion solution, isopropanol, and deionized water in a volumetric ratio of 0.125:1:4). The mixture was sonicated for at least 30 min to form a homogeneous ink. Subsequently, 200 μL of Ru/C ink was drop-cast onto both sides of the CC.

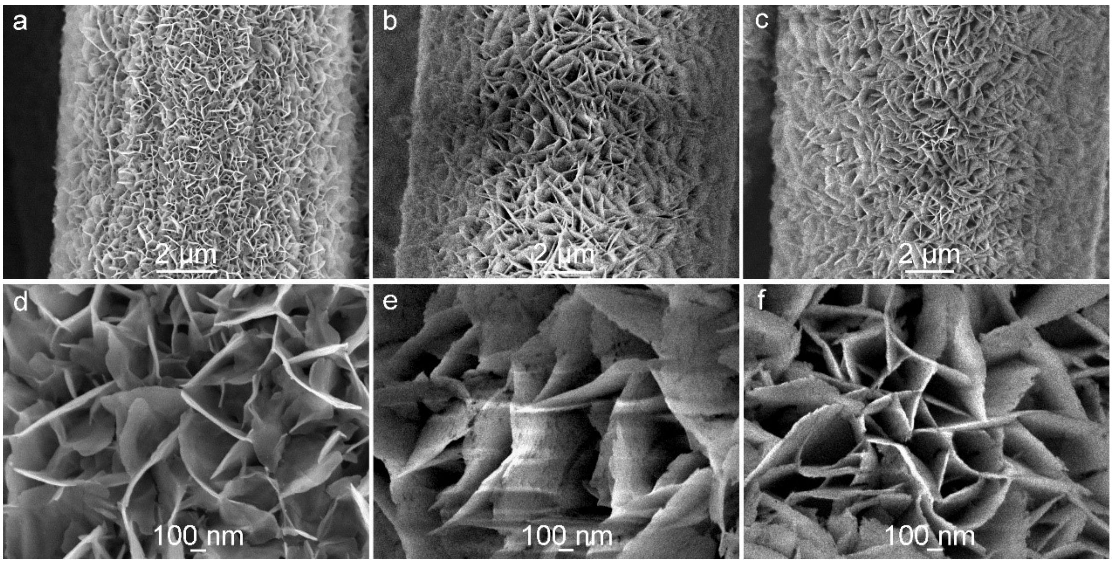

Fig. S20. SEM images of (a, d) Pd-$Co(OH)_2$/CC, (b, e) Ir-$Co(OH)_2$/CC, and (c, f) Rh-$Co(OH)_2$/CC.

A piece of $Co(OH)_2$/CC (2×3 cm^2) was immersed in 20 mL of 5 mM aqueous solution of the corresponding metal precursor—$IrCl_3 \cdot xH_2O$ for Ir-$Co(OH)_2$, $PdCl_2$ for Pd-$Co(OH)_2$, and $RhCl_3 \cdot xH_2O$ for Rh-$Co(OH)_2$—for 20 minutes. The resulting materials were then thoroughly rinsed with deionized water and dried at 70 °C overnight.

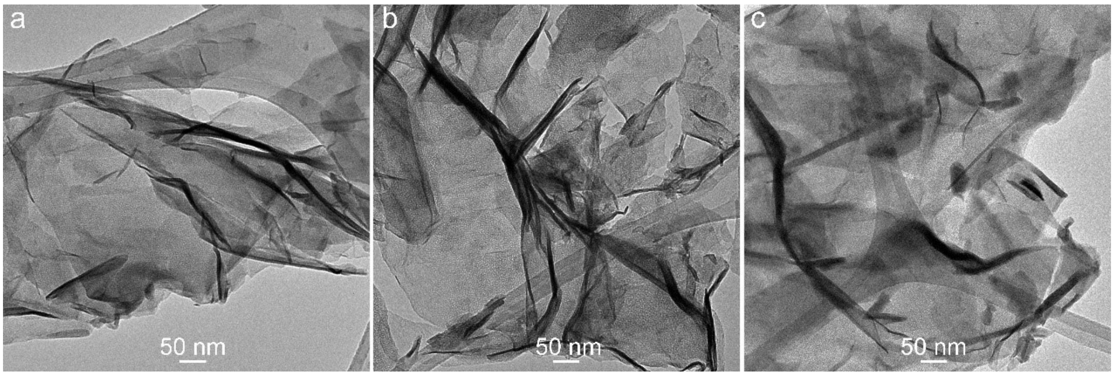

Fig. S21. TEM images of (a) Pd-Co$(OH)_2$, (b) Ir-Co$(OH)_2$, and (c) Rh-Co$(OH)_2$.

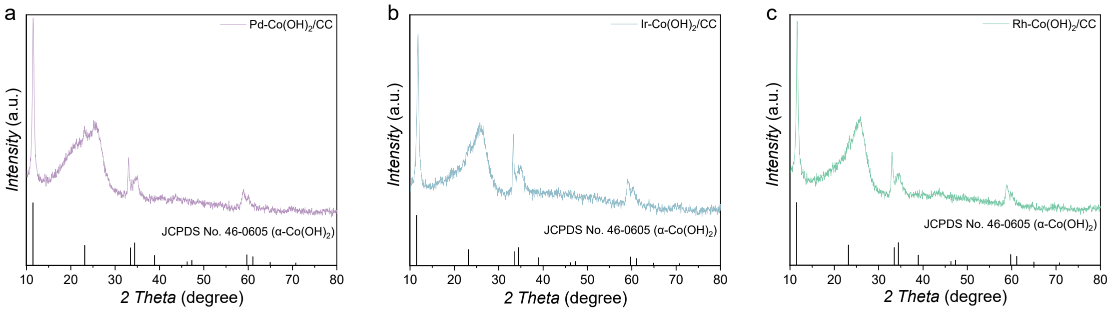

Fig. S22. XRD patterns of (a) Pd-Co(OH)$_2$/CC, (b) Ir-Co(OH)$_2$/CC, and (c) Rh-Co(OH)$_2$/CC.

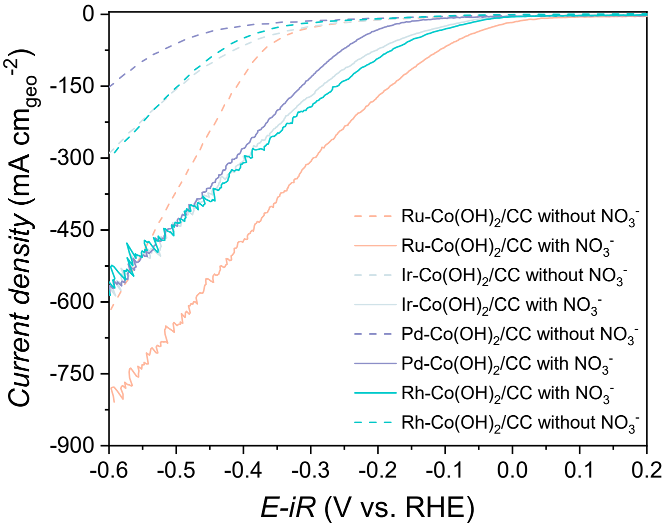

Fig. S23. LSV curves of Pd-$Co(OH)_2$/CC, Ir-$Co(OH)_2$/CC, Rh-$Co(OH)_2$/CC, and Ru-$Co(OH)_2$/CC in Ar-saturated 1 M KOH solution with and without 2,000 ppm NO_3^-.

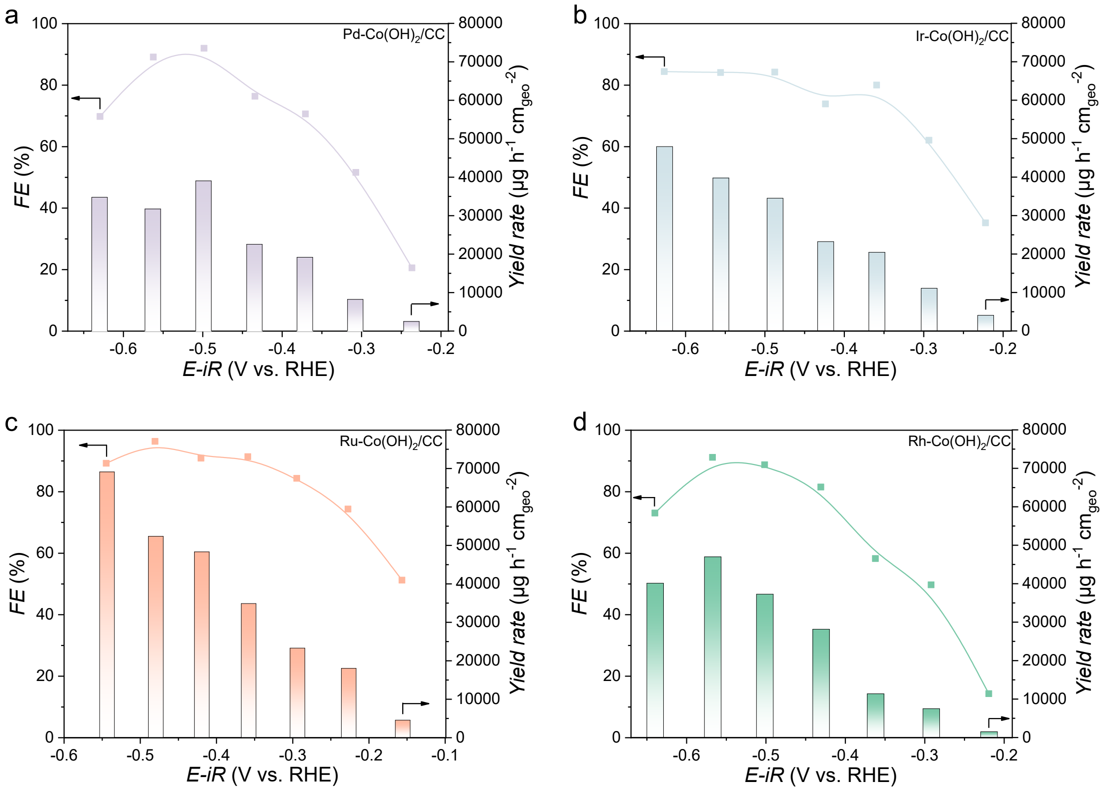

Fig. S24. NH_3 yield rates and FEs of (a) Pd-Co(OH)$_2$/CC, (b) Ir-Co(OH)$_2$/CC, (c) Ru-Co(OH)$_2$/CC, and (d) Rh-Co(OH)$_2$/CC in 1 M KOH solution with 2,000 ppm NO_3^-.

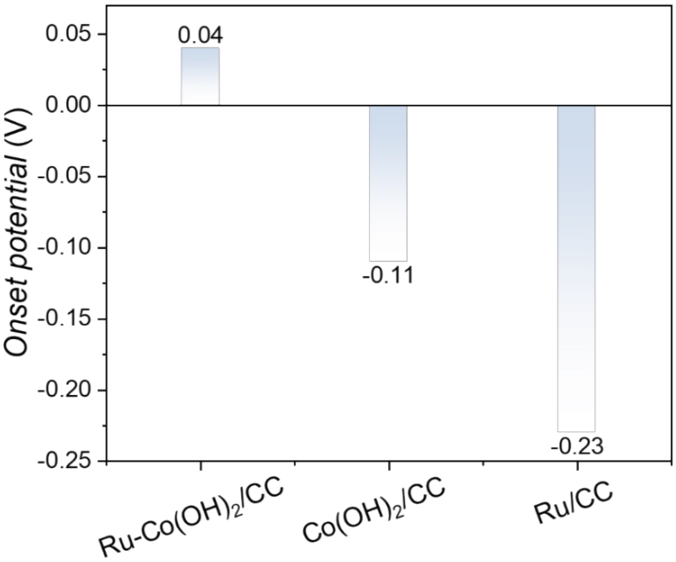

Fig. S25. Onset potential of Ru-$Co(OH)_2$/CC, $Co(OH)_2$/CC, and Ru/CC for NO_3RR in Ar-saturated 1 M KOH solution with 2,000 ppm NO_3^-.

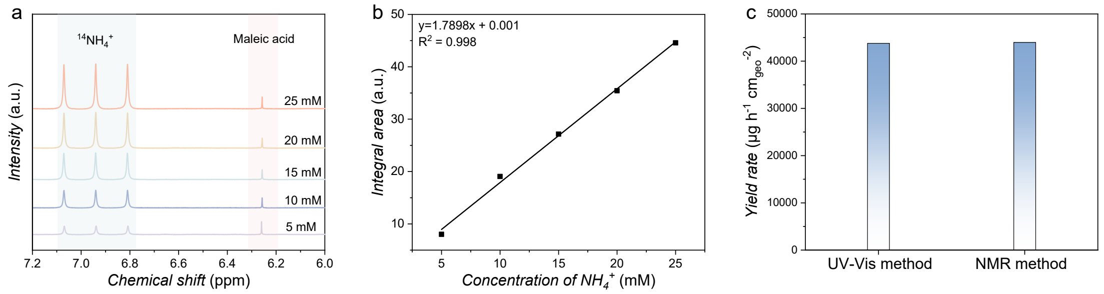

Fig. S26. Standard curve of $^{14}NH_4^+$ quantification by ^1H NMR. (a) ^1H NMR spectra of $^{14}NH_4$ at different concentrations and (b) the corresponding standard curve. (c) NH_3 yield rates determined by ^1H-NMR spectroscopy and UV-Vis spectroscopy of Ru-Co(OH)$_2$/CC at –0.48 V vs. RHE in 1 M KOH solution with 2,000 ppm NO_3^-.

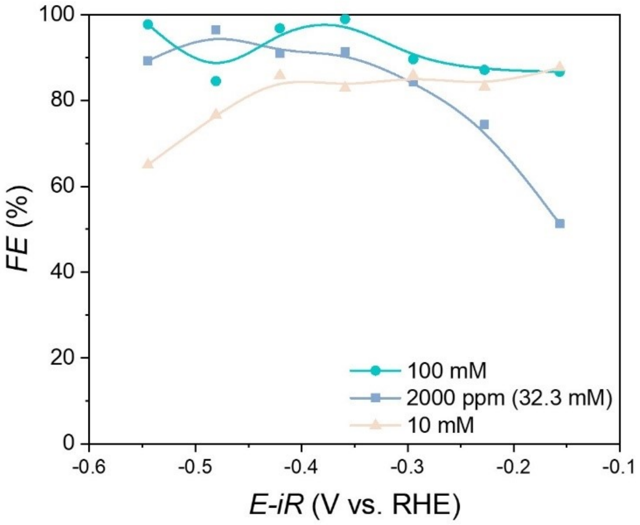

Fig. S27. NH_3 FEs of Ru-$Co(OH)_2$/CC in Ar-saturated 1 M KOH solution with different NO_3^- concentration.

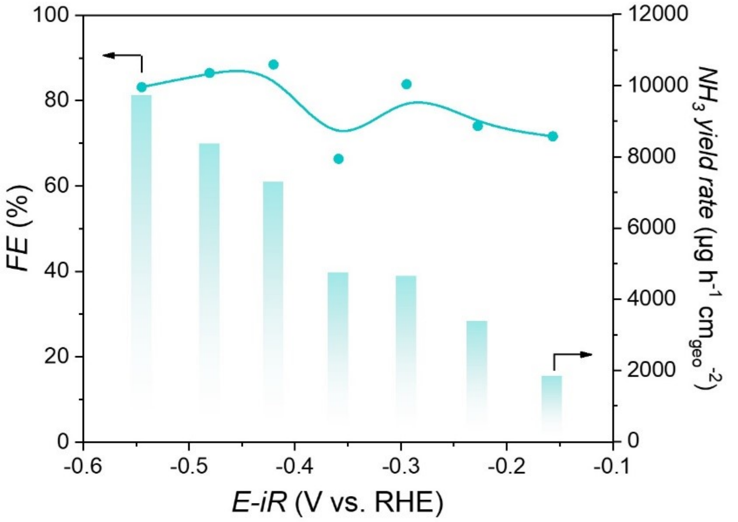

Fig. S28. NH_3 yield rates and FEs of Ru-Co(OH)$_2$/CC in Ar-saturated 0.05 M Na_2SO_4 solution with 2,000 ppm NO_3^-.

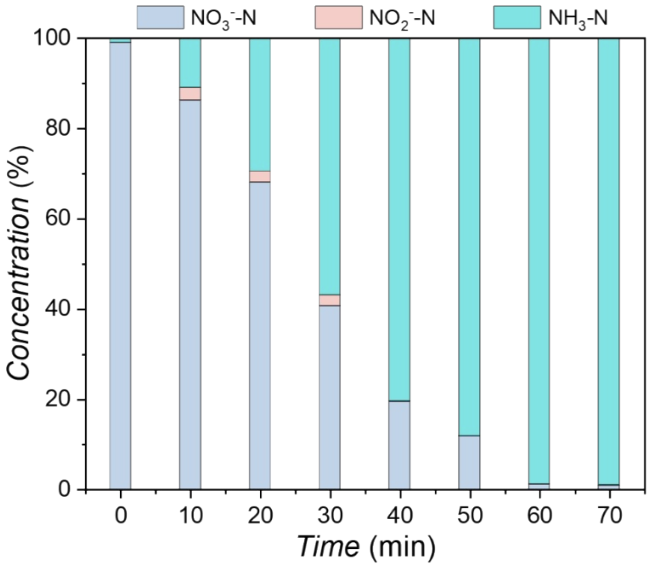

Fig. S29. Product ratios at different times using Ru-Co(OH)$_2$/CC as the catalyst for complete NO_3^- conversion. The cell is operated under –0.48 V vs. RHE with an initial 2,000 ppm NO_3^- in Ar-saturated 1 M KOH solution.

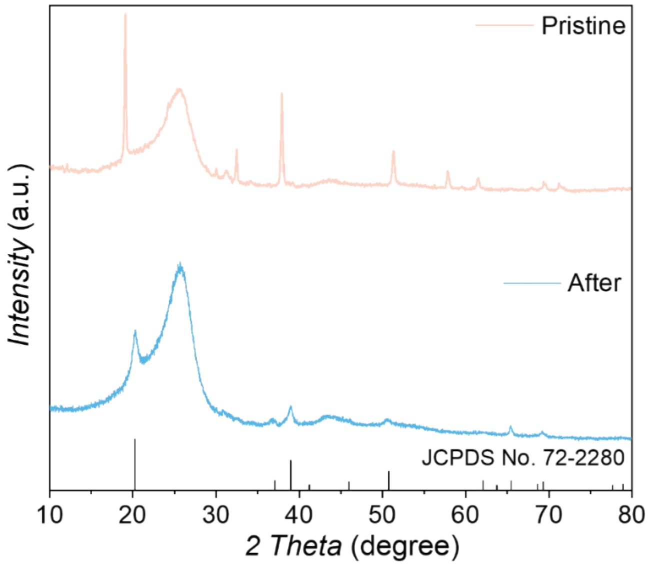

Fig. S30. XRD patterns of pristine and post-NO_3RR Ru-$Co(OH)_2$/CC in Ar-saturated 1 M KOH solution with 2,000 ppm NO_3^-.

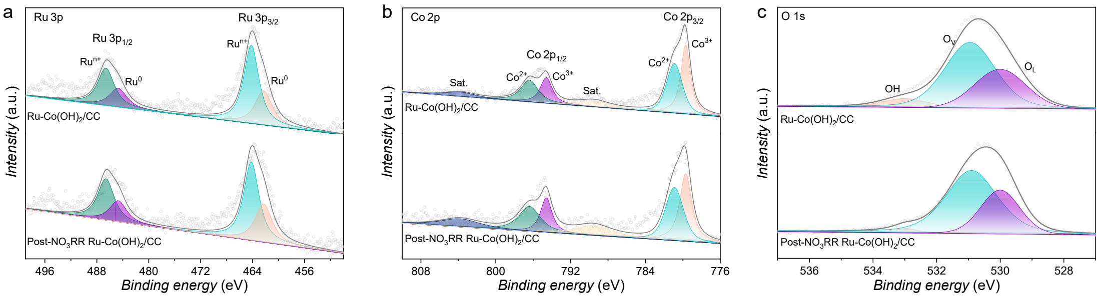

Fig. S31. High-resolution X-ray photoelectron spectra of pristine and post-NO$_3$RR Ru-Co(OH)$_2$/CC in Ar-saturated 1 M KOH solution with 2,000 ppm NO$_3^-$.

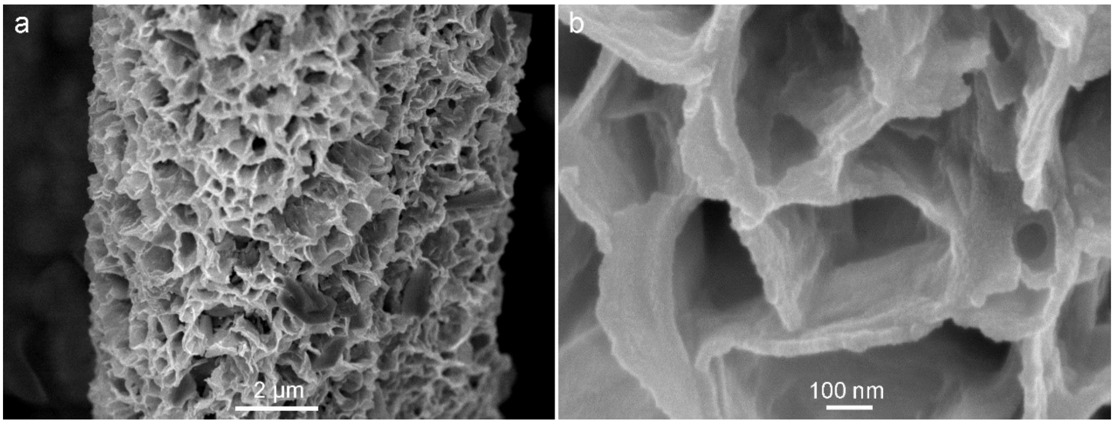

Fig. S32. (a) Low- and (b) high-magnification SEM images of post-NO_3RR Ru-$Co(OH)_2$/CC in Ar-saturated 1 M KOH solution with 2,000 ppm NO_3^-.

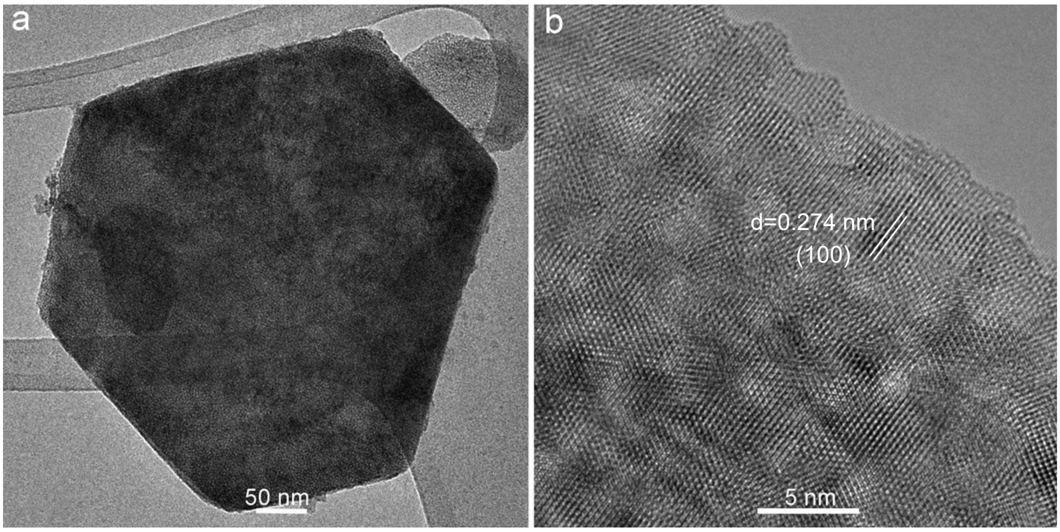

Fig. S33. (a) TEM and (b) HRTEM images of post-NO_3RR Ru-$Co(OH)_2$/CC in Ar-saturated 1 M KOH solution with 2,000 ppm NO_3^-.

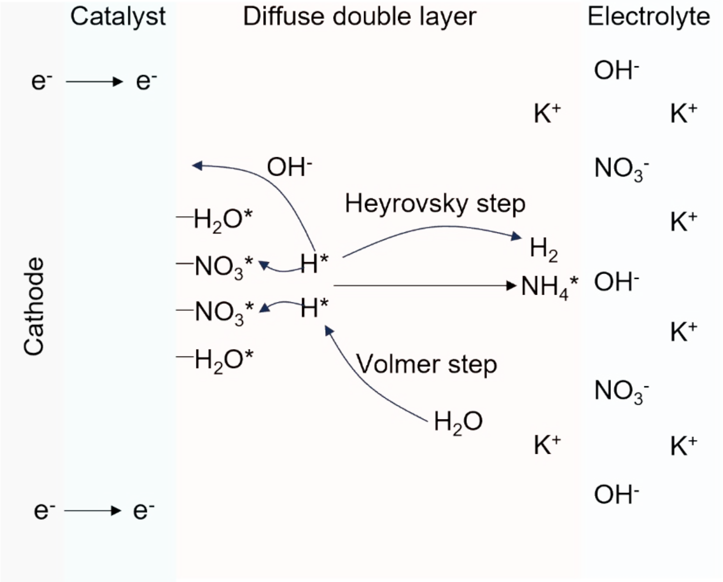

Fig. S34. Equivalent circuit model used in fitting the electrochemical impedance spectra and schematic diagram of the proposed reaction mechanism over Ru-$Co(OH)_2$/CC.

The cathodic resistance consists of four components: (i) resistance to electron transfer from the cathode to the catalytic sites; (ii) resistance associated with the adsorption of intermediates at the reaction interface; (iii) resistance to electron transfer from the reaction interface to the intermediates; and (iv) diffusion resistance of products in the electrolyte.[13,14]

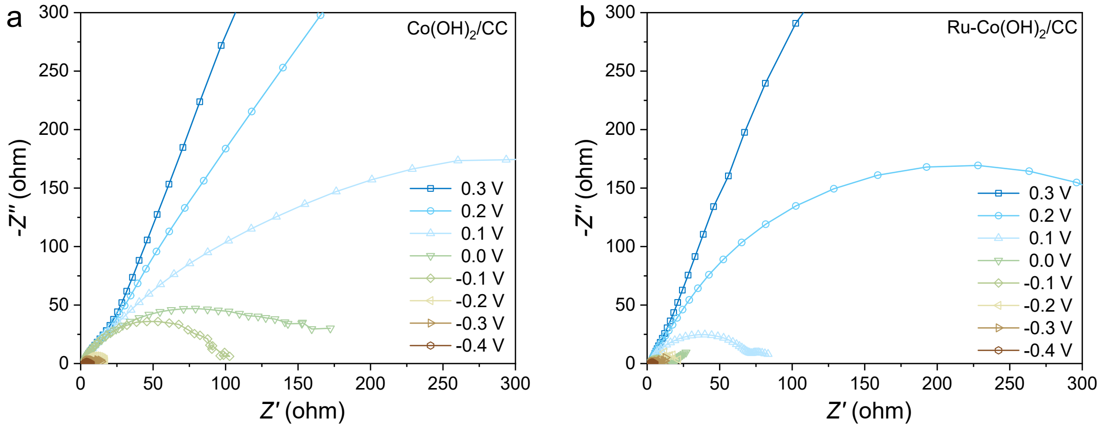

Fig. S35. Nyquist plots of (a) Co(OH)$_2$/CC and (b) Ru-Co(OH)$_2$/CC in Ar-saturated 1 M KOH solution with 2,000 ppm NO_3^-.

The Nyquist spectra of Co(OH)$_2$/CC exhibited nearly oblique lines at low potentials from 0.3 V to 0.2 V vs. RHE in Ar-saturated 1 M KOH solution with 2,000 ppm NO_3^-, suggesting high resistance at the interface between the electrode and electrolyte (Fig. S35a). Notably, the charge-transfer resistance of Ru-Co(OH)$_2$/CC in Ar-saturated 1 M KOH solution with 2,000 ppm NO_3^- was significantly smaller than that of Co(OH)$_2$/CC under the same bias (Fig. S35b).

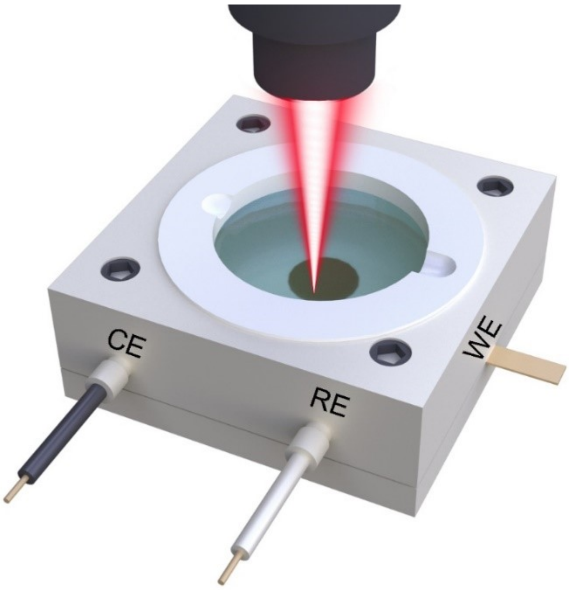

Fig. S36. Schematic of a custom in situ electrochemical Raman cell.

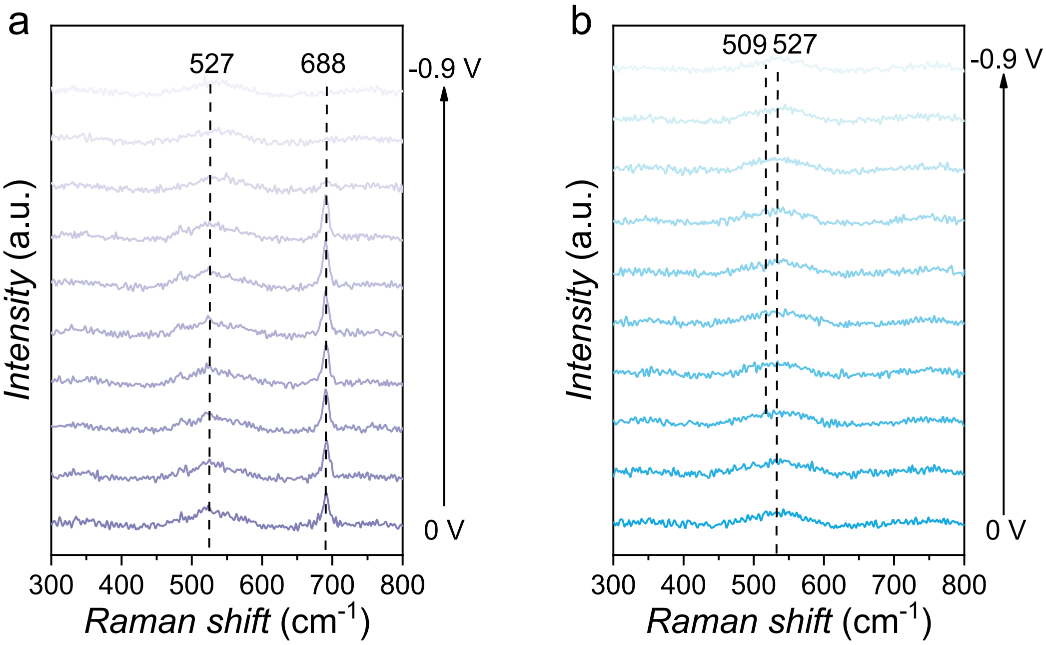

Fig. S37. In situ Raman spectra of (a) $Co(OH)_2$/CC and (b) Ru-$Co(OH)_2$/CC in Ar-saturated 1 M KOH solution at a series of applied potentials.

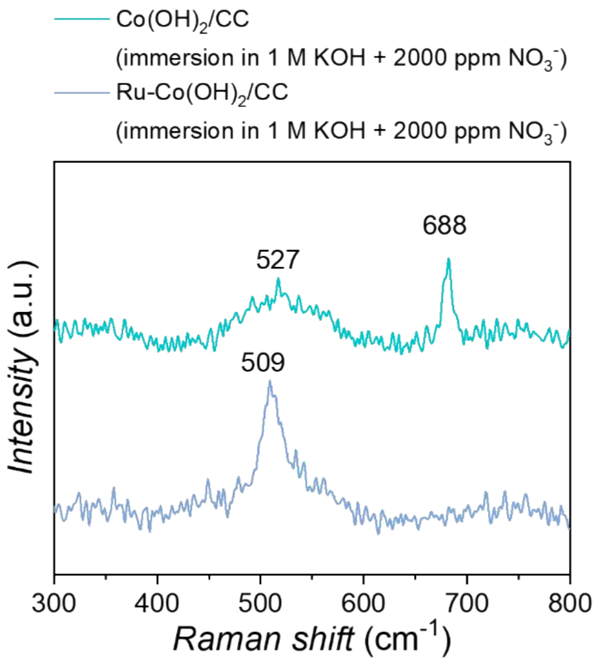

Fig. S38. Raman spectra of $Co(OH)_2$/CC and Ru-$Co(OH)_2$/CC immersed in 1 M KOH solution with 2,000 ppm NO_3^-.

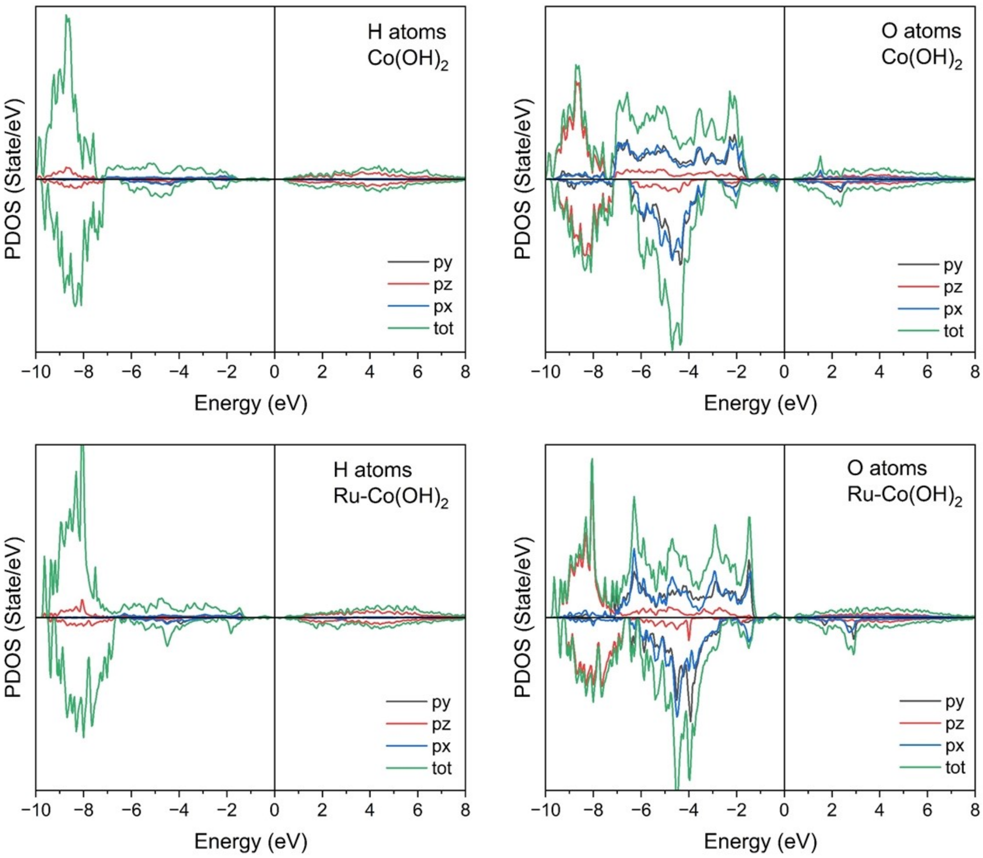

Fig. S39. Partial density of states of H and O atoms of $Co(OH)_2$ and Ru-$Co(OH)_2$.

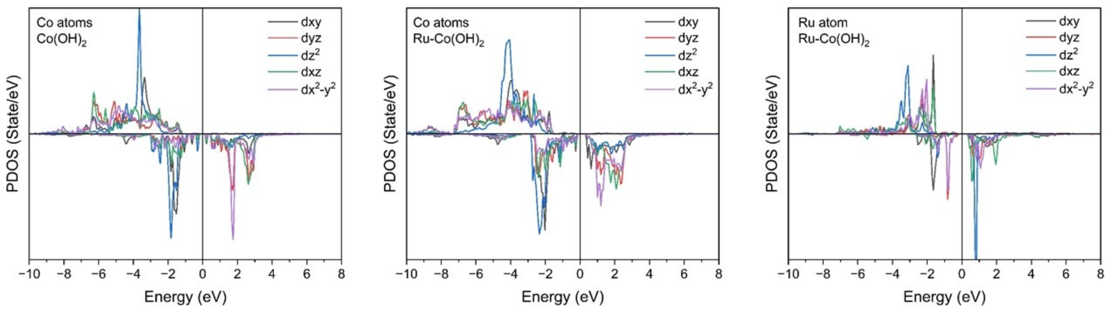

Fig. S40. Partial density of states of Co and Ru atoms of Co(OH)$_2$ and Ru-Co(OH)$_2$.

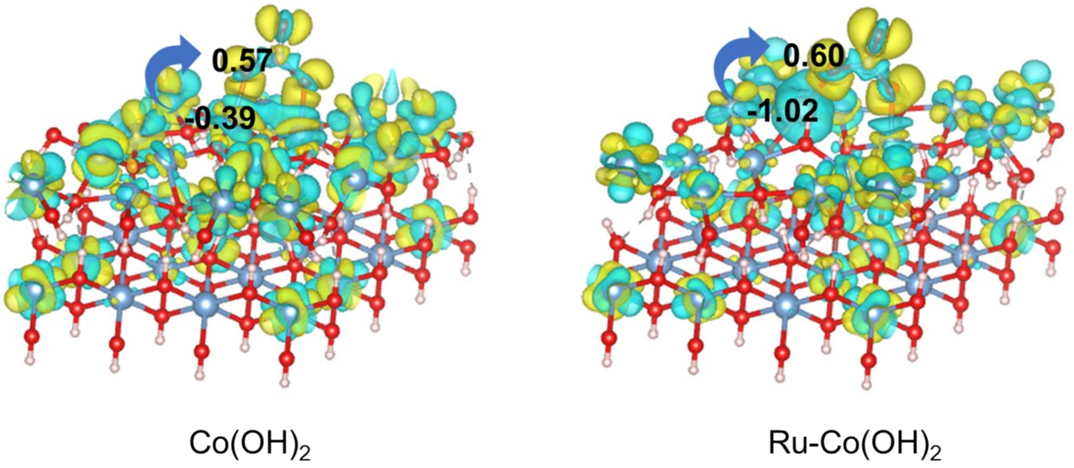

Fig. S41. Difference charge density and Bader of $*NO_3$ of $Co(OH)_2$ and Ru-$Co(OH)_2$, isosurface level is 0.02 e/Å^3.

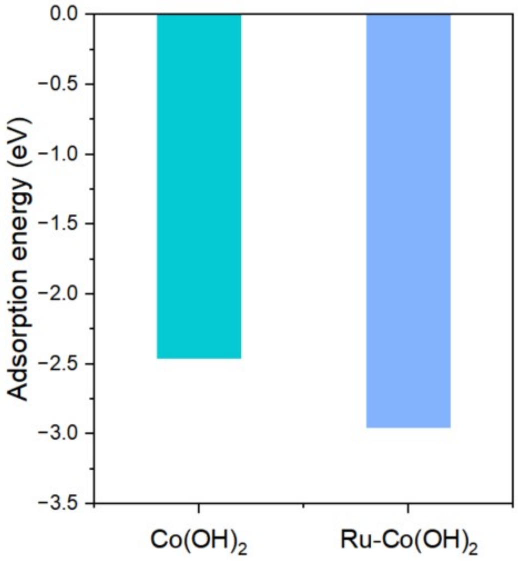

Fig. S42. The NO_3^- adsorption energy of $Co(OH)_2$ and $Ru\text{-}Co(OH)_2$.

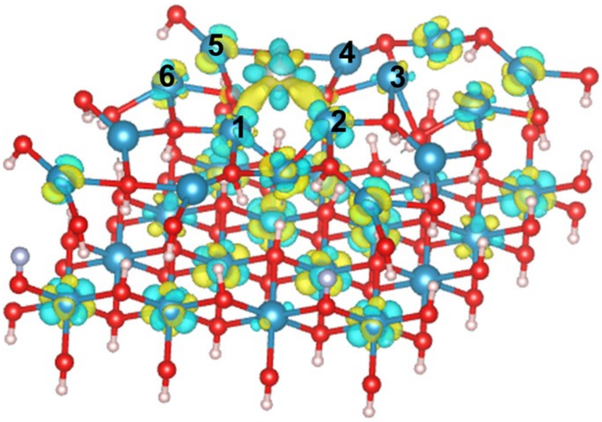

Fig. S43. Difference charge density of Ru-Co(OH)$_2$, isosurface level is 0.1 e/Å^3.

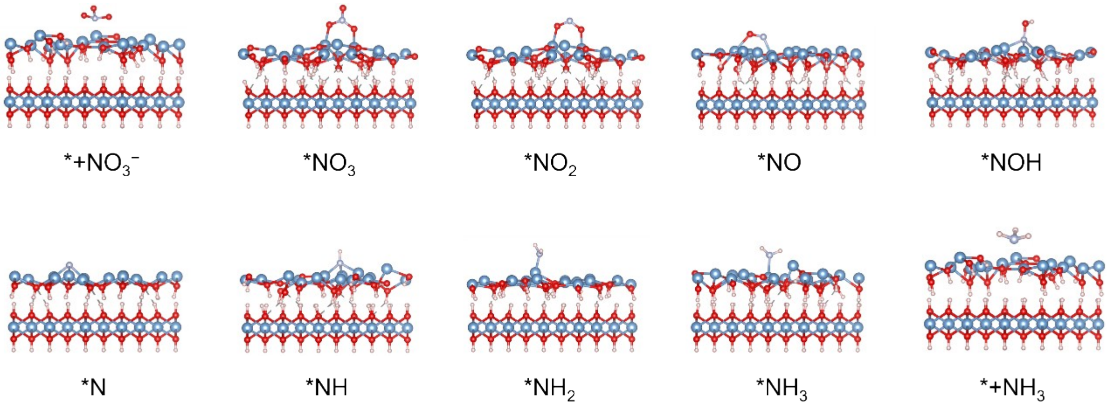

*+NO_3^- *NO_3 *NO_2 *NO *NOH

*N *NH *NH_2 *NH_3 *+NH_3

Fig. S44. Lattice structure of $Co(OH)_2$ for NO_3RR.

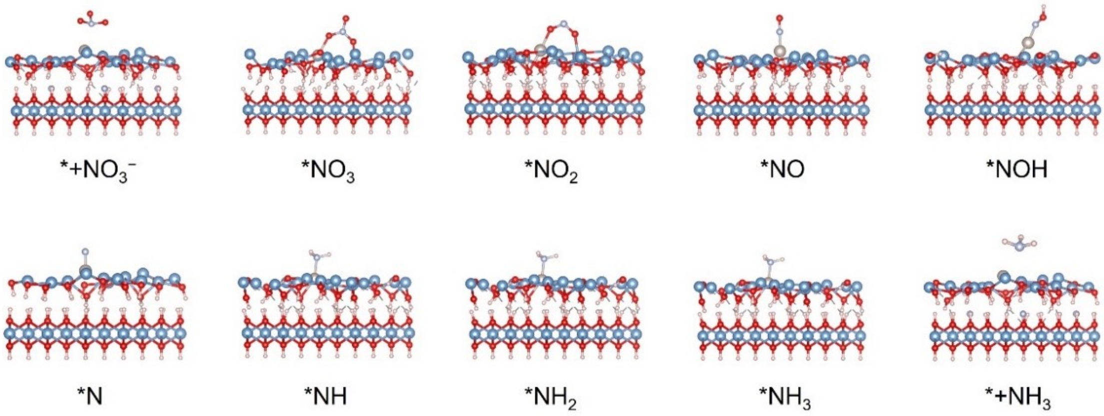

Fig. S45. Lattice structure of Ru-$Co(OH)_2$ for NO_3RR.

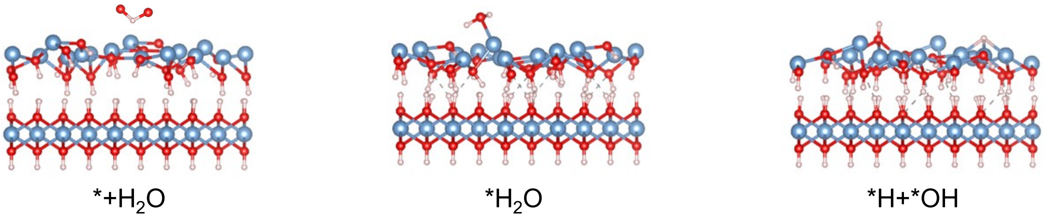

Fig. S46. Lattice structure of $Co(OH)_2$ for hydrogen evolution reaction.

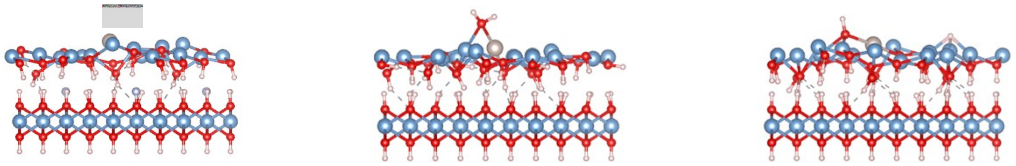

$*+H_2O$ $*H_2O$ $*H+*OH$

Fig. S47. Lattice structure of Ru-$Co(OH)_2$ for hydrogen evolution reaction.

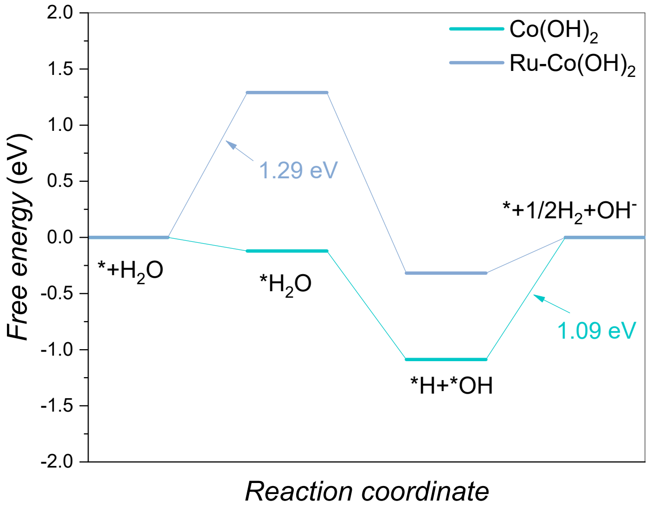

Fig. S48. Reaction free-energy diagram of $Co(OH)_2$ and Ru-$Co(OH)_2$ for hydrogen evolution reaction.

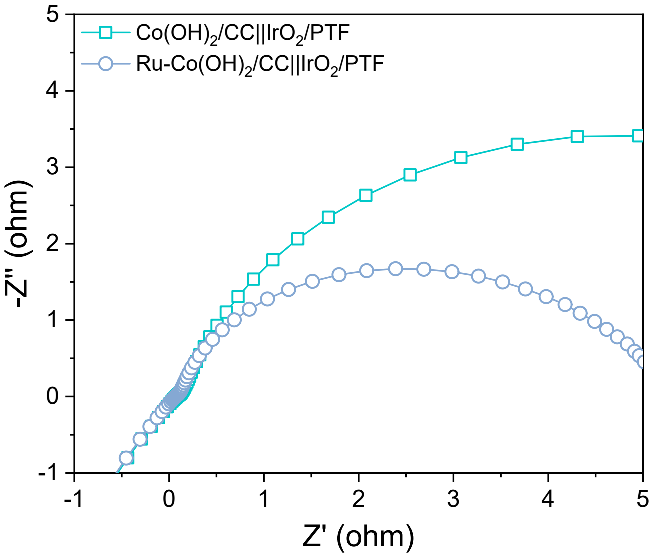

Fig. S49. Electrochemical impedance spectroscopy plots of the MEA cell with Ru-$Co(OH)_2$/CC and $Co(OH)_2$/CC cathodes, paired with an IrO_2/PTF anode.

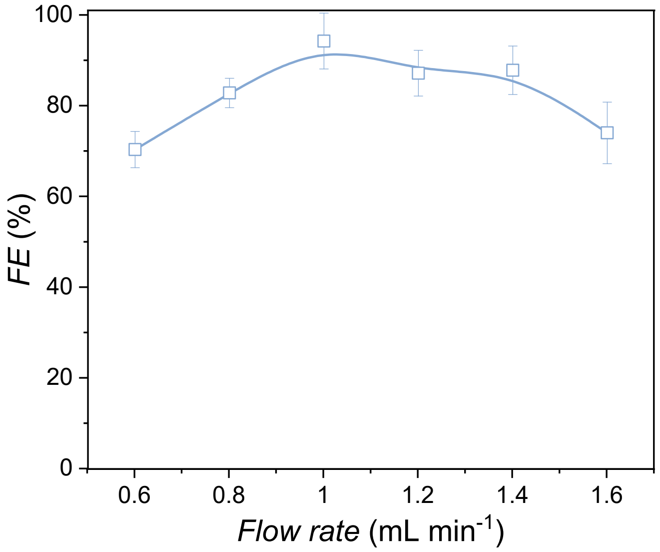

Fig. S50. FEs of NH_3 at a current density of 100 mA cm^{-2} under different flow rates in the MEA setup.

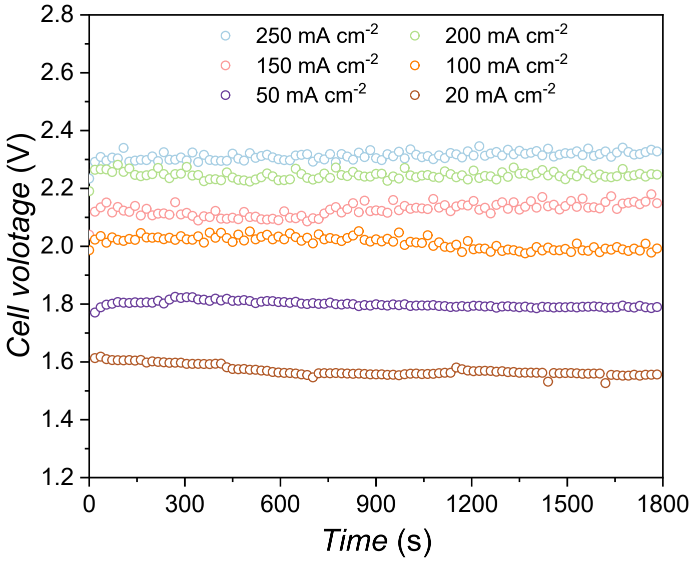

Fig. S51. Cell voltage profiles during 30-min constant-current electrolysis for the MEA system at different current densities.

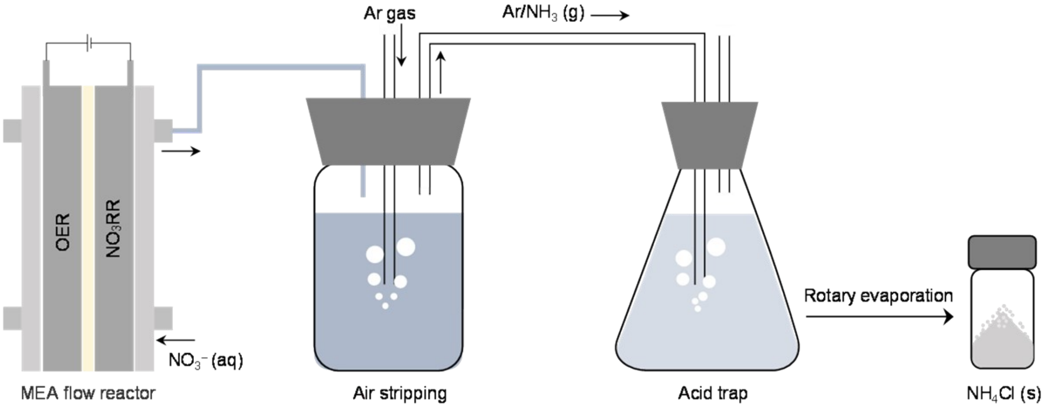

Fig. S52. Schematic of the NH_3 product synthesis process from NO_3^--containing influent to NH_4Cl (s).

The process for collecting NH_4Cl product is schematically depicted. Following the NO_3RR tests conducted at a current density of 100 mA cm^{-2}, 200 mL of cathodic electrolyte was transferred to a conical flask. To recover the dissolved and volatilized ammonia, Ar gas (100 sccm) was bubbled continuously through the electrolyte at 70 °C for 12 h. This stripping step ensured complete release of NH_3 from the alkaline solution. The outflowing gas stream was directed into an acid trap containing 200 mL of 0.3 M HCl, where the NH_3 was efficiently captured and converted into NH_4^+. This acid-trapping method was crucial for minimizing ammonia loss due to volatilization and ensuring accurate quantification of the reaction product. The collected solution was subsequently concentrated by rotary evaporation at 70 °C for 3 h, followed by overnight drying in an oven to yield the final NH_4Cl powder.

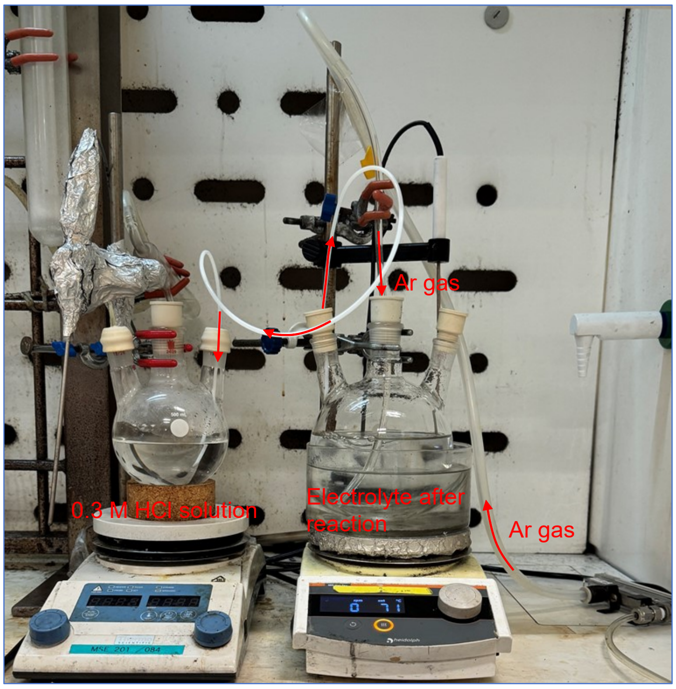

Fig. S53. Photo of trapping gas-phase NH_3 in 0.3 M HCl solution via air stripping.

Fig. S54. Photo of the removal of water from the product using a rotary evaporator at 70 °C.

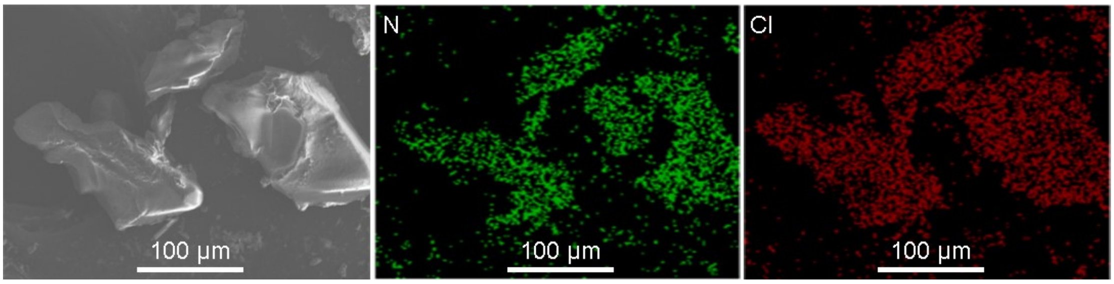

Fig. S55. Elemental mapping images confirm the homogeneous distribution of N and Cl elements in the dried precipitate.

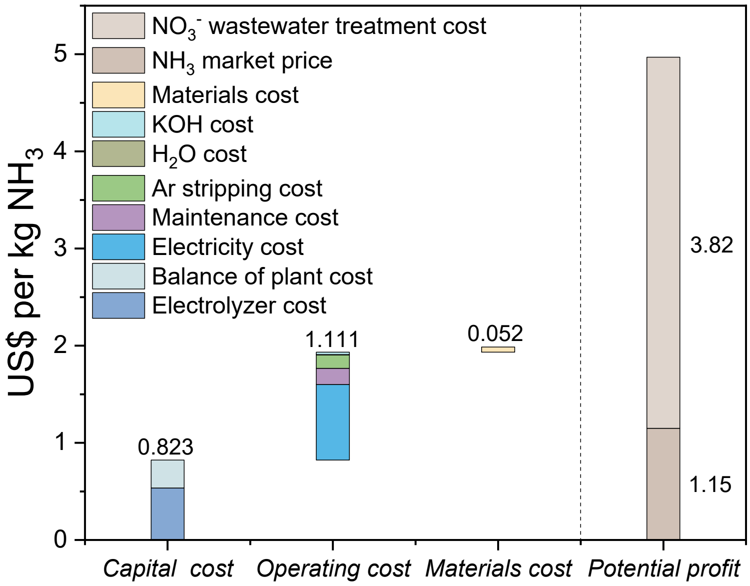

Fig. S56. Breakdown of the production cost and potential profitability of NH_3 synthesis via NO_3RR using a MEA reactor.

The total production cost, encompassing capital, operating, and materials costs, is estimated at US$1.986 per kg NH_3. Potential profit considerations include selling NH_3 at the current market price[15] and cost savings from water treatment plants for nitrogen waste processing.[16,17]

Despite a higher production cost compared to NH_3 synthesized via the Haber–Bosch process (US$1.15 per kg NH_3), the electrochemical NO_3^- conversion could become economically competitive when accounting for the offset costs of NO_3^- wastewater treatment (US$65 per kmol N, equivalent to US$3.82 per kg NH_3). This co-production approach could position the process within a viable economic range for integrated wastewater management and NH_3 synthesis.

Note S1 Techno-economic assessment of NO_3^- conversion using MEA reactor.

TEA in this study was developed and conducted based on previously reported models.[18,19] The baseline parameters for NO_3RR in the MEA reactor were selected based on the performances in this study: a current density of 100 mA cm^{-2}, a total cell voltage of 1.95 V, and an NH_3 FE of 94.2%. Targeted comparison cases include traditional Haber-Bosch plants (reflected by NH_3 market price[20] and the NO_3^- wastewater treatment cost.[16,21]

Power needed

Assuming an NH_3 production rate of 1000 kg day^{-1}, the total current needed is:

$$Total\ current = 1000\frac{kg}{day} \times \frac{day}{86400s} \times \frac{kmol}{17.031kg} \times \frac{1000mol}{kmol} \times 8e^- \times \frac{96485C}{mol} \times \frac{1}{94.2\%} =$$

The total electrolyzer area needed is:

$$Total\ electrolyzer\ area = \frac{556858\ A}{0.1\ A\ cm^{-2}} \times \frac{m^2}{10^4\ cm^2} = 556.8\ m^2\ (2)$$

The power needed is calculated by P=UI

$$Total\ power\ needed = 1.95\ V \times 556858\ A \times \frac{MW}{10^6\ W} = 1.08\ MW\ (3)$$

Resources needed

1. The NO_3^- treated per day is:

$$NO_3^-\ needed = 1000\frac{kg(NH_3)}{day} \times \frac{1\ kmol}{17.031\ kg(NH_3)} \times \frac{62\ kg(NO_3^-)}{1\ kmol} = 3640.4\frac{kg}{day}\ (4)$$

2. The water flow rate needed for anodic OER is:

$$H_2O = 556859\ A \times \frac{1}{4e^- \times \frac{96485\ C}{mol}} \times \frac{0.018\ kg}{mol} \times \frac{0.2642\ gal}{kg} \times \frac{86400\ s}{day} = 592\frac{gal}{day}\ (5)$$

Capital cost

1. Electrolyzer cost

Based on the E4tech/Element Energy report and DOE H2A analysis for central grid electrolysis,[22,23] the electrolyzer cost for the stack component is 550 USD kW^{-1} with a reference current density of 400 mA cm^{-2} at 1.75 V. An installation factor of 1.12 was used for the capital investment.[23] The total electrolyzer cost is calculated as:

$$Electrolyzer\ cost = \frac{550\ \$\ kW^{-1}}{1000\frac{W}{kW}} \times \frac{400\ mA\ cm^{-2}}{1000\frac{mA}{A}} \times 1.75\ V \times \frac{556.8\ m^2}{0.0001\frac{m^2}{cm^2}} \times 1.12 = \$2400921\ (6)$$

Considering the capital recovery factor (CRF) based on a 5% discount rate (denote as i in the equation below), with the lifetime of 20 years:

$$CRF = \frac{i(1+i)^{year}}{(1+i)^{year} - 1} = 0.0802\ (7)$$

With the operation of 360 days per year and NH_3 production rate of 1000 kg day^{-1}, the electrolyzer cost per kg of NH_3 is:

$$Electrolyzer\ cost = \$2400921 \times \frac{0.0802}{360\ day} \times \frac{1}{1000\ kg\ day^{-1}} = 0.535\ \$\ kg(NH_3)^{-1}\ (8)$$

2. Balance of plant (BoP) cost

The BoP cost is assumed to be 35% of the total cost of the electrolyzer system,[18,23] which is:

$$BoP\ cost = \frac{0.535\ \$\ kg(NH_3)^{-1}}{65\%} \times 35\% = 0.288\ \$\ kg(NH_3)^{-1}\ (9)$$

Operating cost

1. Electricity cost

The electricity cost is calculated from the power requirement and an electricity price of 3 cent kWh^{-1} based on the target announced by DOE.[24,25]

$$Electricity\ cost = 1.08\ MW \times \frac{1000\ kW}{MW} \times 24\ h \times \frac{\$\ 0.03}{kWh} \times \frac{1}{1000\ kg\ day^{-1}} = 0.777\ \$\ kg(NH$$

2. Maintenance

It is assumed that maintenance costs are 2.5% of the capital electrolyzer cost per year.[18,23]

$$Maintenance = \$\ 2400921 \times \frac{2.5\%}{year} \times \frac{year}{360\ days} \times \frac{1}{1000\ kg\ day^{-1}} = 0.167\ \$\ kg(NH_3)^{-1}\ (11)$$

3. Water cost

The cost of water to support the anodic OER with the price of \$0.0054 gal^{-1}:

$$H_2O\ cost = \frac{592\ gal}{day} \times \frac{\$0.0054}{gal} \times \frac{1}{1000\ kg\ day^{-1}} = 0.003\ \$\ (NH_3)^{-1}\ (12)$$

4. KOH cost

In addition, we assume the KOH cost is 5% of the electrolyzer cost:

$KOH\ cost = 0.535\ \$\ kg(NH_3)^{-1} \times 5\% = 0.026\ \$\ kg(NH_3)^{-1}$ (13)

5. Air stripping cost

NH_3 air stripping cost is calculated with the reference of 5.6 kWh $kg(N)^{-1}$ and the electricity price of 3 cent per kWh[26]:

$$\begin{aligned} &Air\ stripping\ cost \\ &= 1000\ kg\ day^{-1} \times \frac{1\ kmol}{17.031\ kg(NH_3)} \times \frac{14\ kg(N)}{1\ kmol} \times \frac{5.6\ kWh}{kg(N)^{-1}} \times \frac{\$0.03}{kWh} \times \frac{}{100} \\ &= 0.138\ \$\ kg\ (NH_3)^{-1} (14) \end{aligned}$$

Materials cost

we assume the materials cost is 10% of the electrolyzer cost[18,23]:

$Materials\ cost = 0.535\ \$\ kg(NH_3)^{-1} \times 10\% = 0.052\ \$\ kg(NH_3)^{-1}$ (15)

6. Electrodialysis cost for concentrating NO_3^- sources

In the scenario where NO_3^- is required to concentrated by electrodialysis in advance before feeding into MEA system, the cost of electrodialysis process is calculated with the reference of US\$5.75 (kmol(NO_3^-)$^{-1}$) total process cost that concentrated the NO_3^- from 7.14 mM to 2 M of wastewater sources[13]. The electrodialysis cost to supply the NO_3^- need of 3640.4 kg day^{-1} for MEA system is calculated as:

$$\begin{aligned} &Electrodialysis\ process\ cost\ for\ NO_3^- \\ &= 3640.4 \frac{kg}{day} \times \frac{\$5.75}{kmol} \times \frac{1\ kmol}{62\ kg} \times \frac{1}{1000\ kg\ day^{-1}} = 0.338\ \$\ kg\ (NH_3)^{-1} (16) \end{aligned}$$

Note that based on the same electrodialysis model[16], if we aim to concentrate the nitrate sources such as municipal wastewater or polluted groundwater[27] from 50 ppm NO_3^- (equivalent to 0.81 mM NO_3^-) to 0.0323 mM (concentration in this work), a total electrodialysis cost would be US\$36.95 (kmol(NO_3^-)$^{-1}$), including US\$6.61 (kmol(NO_3^-)$^{-1}$) of OPEX and US\$30.34 (kmol(NO_3^-)$^{-1}$) of levelized capital cost, which is ~6.4 times higher than the electrodialysis cost above.

Table S1. Comparison of NO_3RR performances of Ru-Co(OH)$_2$/CC with recently reported electrocatalysts.

Electrocatalyst	**Electrolyte**	**NH_3 FE**	**EE**	**NH_3 yield rate**	**NH_3 partial current**	**Ref.**
Ru-Co(OH)$_2$/CC	**0.032 M NO_3^- + 1 M KOH**	**~96%**	**30.4%**	**~56501 μg h^{-1} cm^{-2}**	**602.8 mA cm^{-2}**	This work
	0.1 M NO_3^- + 1 M KOH	**97.2%**	**30.2%**	**84413.5 μg h^{-1} cm^{-2}**	**901.2 mA cm^{-2}**	
CuCo NW	0.032 M NO_3^- + 0.1 M KOH	92.7%	14.67%	7310 μg h^{-1} cm^{-2}	444.9 mA cm^{-2}	28
Cu_1Ru_{100}	0.01 M NO_3^- + 0.1 M KOH	48%	21.79%	2380 μg h^{-1} cm^{-2}	102 mA cm^{-2}	29
Cu/β-Co(OH)$_2$	0.1 M NO_3^- + 0.1 M KOH	97.7%	/	66300 μg h^{-1} cm^{-2}	882 mA cm^{-2}	30
P-Cu/Co(OH)$_2$	0.1 M NO_3^- + 1 M KOH	97.04%	/	42630 μg h^{-1} cm^{-1}	1315 mA cm^{-2}	31
Ru-Cu nanowire	0.032 M NO_3^- + 1 M KOH	96.0%	/	76500 μg h^{-1} cm^{-2}	965 mA cm^{-2}	32
CuCo/CN	0.032 M NO_3^- + 1 M KOH	93.56 %	/	3967.8 μg h^{-1} cm^{-2}	185 mA cm^{-2}	33
NG-RuCo	0.032 M NO_3^- + 1 M KOH	93%	/	81600 μg h^{-1} cm^{-2}	810 mA cm^{-2}	34
CuCoSP	0.01 M NO_3^- + 0.1 M KOH	93.3% ± 2.1%	/	19890 μg h^{-1} cm^{-2}	38 mA cm^{-2}	35
Cu_3P@Co(OH)$_2$/CF	0.01 M NO_3^- + 1 M KOH	86.7%	/	3230 μg h^{-1} cm^{-2}	32.4 mA cm^{-2}	36
$CoCuO_x$@CuO_x/CF	0.02 M NO_3^- + 0.1 M KOH	91%	/	32500 μg h^{-1} cm^{-2}	13.6 mA cm^{-2}	37
MP-Cu	0.05 M NO_3^- + 1 M KOH	99.8%	/	9231 μg h^{-1} cm^{-2}	135 mA cm^{-2}	38
CoO_x nanosheets	0.1 M NO_3^- + 0.1 M KOH	93.4% ± 3.8%	/	82400 μg h^{-1} mg_{cat}^{-1}	2.6 mA cm^{-2}	39
Fe/Cu diatomic catalyst/nitrogen-doped graphene	0.1 M NO_3^- + 1 M KOH	92.51%	/	2310 μg h^{-1} cm^{-2}	37 mA cm^{-2}	40
Cu-N-C single atom catalyst	0.1 M NO_3^- + 0.1 M KOH	84.7%	/	4500 μg h^{-1} cm^{-2}	40.6 mA cm^{-2}	41
Ru_xCu_y/rGO	0.1 M NO_3^- + 1 M KOH	98%	/	6460 μg h^{-1} cm^{-2}	42 mA cm^{-2}	42

CoP-CNS	1 M NO_3^- + 1 M NaOH	93.3%	/	52530 μg h^{-1} cm^{-2}	111 mA cm^{-2}	43

Table S2. The intensity of the peak at 1060 cm^{-1} and 1554 cm^{-1} of $Co(OH)_2$ and Ru-$Co(OH)_2$ at different applied potentials in Ar-saturated 1 M KOH solution with 2,000 ppm NO_3^-.

Applied potentials	**Intensity at 1060 cm^{-1}**	**Intensity at 1554 cm^{-1}**	**I_{1060}/I_{1554}**
Ru-$Co(OH)_2$			
0.0 V	38.94	49.22	0.79
-0.1 V	32.42	48.83	0.66
-0.2 V	33.36	54.29	0.61
-0.3 V	37.76	49.64	0.76
-0.4 V	27.32	45.82	0.59
-0.5 V	30.33	46.96	0.64
-0.6 V	43.73	53.14	0.82
-0.7 V	31.37	46.45	0.67
-0.8 V	30.70	55.97	0.54
-0.9 V	43.68	45.91	0.95
Ru-$Co(OH)_2$			
0.0 V	38.18	58.57	0.65
-0.1 V	36.27	45.20	0.80
-0.2 V	40.64	51.33	0.79
-0.3 V	31.18	40.98	0.76
-0.4 V	42.27	48.01	0.88
-0.5 V	33.33	51.51	0.64
-0.6 V	44.95	50.18	0.89
-0.7 V	35.98	45.70	0.78
-0.8 V	39.92	49.05	0.81
-0.9 V	45.76	40.92	1.11

Table S3. The Bader charges of Ru-$Co(OH)_2$ derived from the DFT calculations.

Atoms	**Formal electron loss**
Co-1	-0.89
Co-2	-0.86
Co-3	-0.48
Co-4	-0.11
Co-5	-0.79
Co-6	-0.78
Ru	0.19

Table S4. The calculated free energy of all intermediates over $Co(OH)_2$ and Ru-$Co(OH)_2$.

Models	**Status**	**ΔG(eV)**	**Free energy (eV)**
$Co(OH)_2$ (001)	$Co(OH)_2$ (001) + NO_3^-	0	0
$*NO_3$	$* + NO_3^- \rightarrow *NO_3$	−2.45874	−2.45874
$*NO_2$	$*NO_3 + 2H \rightarrow *NO_2 + H_2O$	−2.04234	−4.50108
$*NO$	$*NO_2 + 2H \rightarrow *NO + H_2O$	0.785941	−3.71514
$*NOH$	$*NO + H \rightarrow *NOH$	−1.41307	−5.12821
$*N$	$*NOH + H \rightarrow *N + H_2O$	−0.56992	−5.69813
$*NH$	$*N + H \rightarrow *NH$	−2.05133	−7.74945
$*NH_2$	$*NH + H \rightarrow *NH_2$	−0.89961	−8.64907
$*NH_3$	$*NH_2 + H \rightarrow *NH_3$	0.485609	−8.16346
	$*NH_3 \rightarrow * + NH_3$	0.36355	−7.79991
Ru-$Co(OH)_2$ (001)	Ru-$Co(OH)_2$ (001) + NO_3^-	0	0
$*NO_3$	$* + NO_3^- \rightarrow *NO_3$	−2.95435	−2.95435
$*NO_2$	$*NO_3 + 2H \rightarrow *NO_2 + H_2O$	−2.11622	−5.07057
$*NO$	$*NO_2 + 2H \rightarrow *NO + H_2O$	−1.28646	−6.35702
$*NOH$	$*NO + H \rightarrow *NOH$	−0.13116	−6.48818
$*N$	$*NOH + H \rightarrow *N + H_2O$	0.63829	−5.84989
$*NH$	$*N + H \rightarrow *NH$	−0.42026	−6.27016
$*NH_2$	$*NH + H \rightarrow *NH_2$	−1.7307	−8.00086
$*NH_3$	$*NH_2 + H \rightarrow *NH_3$	0.409411	−7.59145
	$*NH_3 \rightarrow * + NH_3$	−0.20846	−7.79991

References

[1] X. Deng, Y. Yang, L. Wang, X.-Z. Fu and J.-L. Luo, *Adv. Sci.*, 2021, **8**, 2004523.

[2] Y. Huang, C. He, C. Cheng, S. Han, M. He, Y. Wang, N. Meng, B. Zhang, Q. Lu and Y. Yu, *Nat. Commun.*, 2023, **14**, 7368.

[3] G. Henkelman, A. Arnaldsson and H. Jónsson, *Comput. Mater. Sci.*, 2006, **36**, 354-360.

[4] S. Kalasina, P. Pattanasattayavong, M. Suksomboon, N. Phattharasupakun, J. Wutthiprom and M. Sawangphruk, *Chem. Commun.*, 2017, **53**, 709-712.

[5] Z. Liu, R. Ma, M. Osada, K. Takada and T. Sasaki, *J. Am. Chem. Soc.*, 2005, **127**, 13869-13874.

[6] T. Deng, W. Zhang, O. Arcelus, J.-G. Kim, J. Carrasco, S. J. Yoo, W. Zheng, J. Wang, H. Tian, H. Zhang, X. Cui and T. Rojo, *Nat. Commun.*, 2017, **8**, 15194.

[7] Q. Zhou, Q. Bian, L. Liao, F. Yu, D. Li, D. Tang and H. Zhou, *Chin. Chem. Lett.*, 2023, **34**, 107248.

[8] K. Kongsawatvoragul, S. Kalasina, P. Kidkhunthod and M. Sawangphruk, *Electrochim. Acta*, 2019, **324**, 134854.

[9] C. C. L. McCrory, S. Jung, J. C. Peters and T. F. Jaramillo, *J. Am. Chem. Soc.*, 2013, **135**, 16977-16987.

[10] D. Zhu, L. Zhang, R. E. Ruther and R. J. Hamers, *Nat. Mater.*, 2013, **12**, 836-841.

[11] L. C. Green, D. A. Wagner, J. Glogowski, P. L. Skipper, J. S. Wishnok and S. R. Tannenbaum, *Anal. Biochem.*, 1982, **126**, 131-138.

[12] Y. Wang, Y. Yu, R. Jia, C. Zhang and B. Zhang, *Natl. Sci. Rev.*, 2019, **6**, 730-738.

[13] Y. Yao, S. Chen, C. Yan, J. Wang, J. Liu, W.-H. Zhu, C. Fan and Z. Guo, *Angew. Chem. Int. Ed.*, 2025, **64**, e202416963.

[14] C. Xie, W. Chen, S. Du, D. Yan, Y. Zhang, J. Chen, B. Liu and S. Wang, *Nano Energy*, 2020, **71**, 104653.

[15] Schnitkey, G. et al. Fertilizer prices and company profits going into spring 2023. Farmdoc Daily https://farmdocdaily.illinois.edu/2023/02/fertilizer-prices-and-company-profits-going-into-spring-2023.html (2023).

[16] Y. Chen, P. Ammari-Azar, H. Liu, J. Lee, Y. Xi, M. J. Castellano, S. Gu and W. Li, *EES Catal.*, 2023, **1**, 504-515.

[17] US EPA. A compilation of cost data associated with the impacts and control of nutrient pollution. https://www.epa.gov/sites/default/files/2015-04/documents/nutrient-economics-report-2015.pdf (2015).

[18] M. Jouny, W. Luc and F. Jiao, *Ind. Eng. Chem. Res.*, 2018, **57**, 2165-2177.

[19] H. Shin, K. U. Hansen and F. Jiao, *Nat. Sustain.*, 2021, **4**, 911-919.

[20] Schnitkey, G. et al. Fertilizer prices and company profits going into spring 2023. farmdoc daily 13, (2023)

[21] USEPA. A compilation of cost data associated with the impacts and control of nutrient pollution. 110 (2015)

[22] Bertuccioli, L. et al. Study on development of water electrolysis in the EU. https://www.fch.europa.eu/sites/default/files/FCHJUElectrolysisStudy_FullReport%20(ID%20199214).pdf. (2014).

[23] James, B., Colella, W., Moton, J. PEM Electrolysis H2A Production Case Study Documentation. https://www.nrel.gov/hydrogen/assets/pdfs/h2a-pem-electrolysis-case-study-documentation.pdf (2013).

[24] Association, U. E. I. Levelized costs of new generation resources in the annual energy outlook 2013. US Department of Energy, January, (2013)

[25] N. M. Haegel, R. Margolis, T. Buonassisi, D. Feldman, A. Froitzheim, R. Garabedian, M. Green, S. Glunz, H.-M. Henning, B. Holder, I. Kaizuka, B. Kroposki, K. Matsubara, S. Niki, K. Sakurai, R. A. Schindler, W. Tumas, E. R. Weber, G. Wilson, M. Woodhouse and S. Kurtz, *Science*, 2017, **356**, 141-143.

[26] C. Shin, A. Szczuka, M. J. Liu, L. Mendoza, R. Jiang, S. H. Tilmans, W. A. Tarpeh, W. A. Mitch and C. S. Criddle, *Environ. Sci. Technol.*, 2022, **56**, 8712-8721.

[27] P. H. van Langevelde, I. Katsounaros and M. T. M. Koper, *Joule*, 2021, **5**, 290-294.

[28] K. Zhang, P. Sun, Y. Huang, M. Tang, X. Zou, Z. Pan, X. Huo, J. Wu, C. Lin, Z. Sun, Y. Wan, X. Zhang and L. An, *Adv. Funct. Mater.*, 2024, **34**, 2405179.

[29] R. Boppella, M. Ahmadi, B. M. Arndt, D. R. Lustig and M. Nazemi, *ACS Catal.*, 2024, **14**, 18223-18236.

[30] L. Qiao, A. Zhu, D. Liu, K. An, J. Feng, C. Liu, K. W. Ng and H. Pan, *Adv. Energy Mater.*, 2024, **14**, 2402805.

[31] Q. Yan, R. Zhao, L. Yu, Z. Zhao, L. Liu and J. Xi, *Adv. Mater.*, 2024, **36**, 2408680.

[32] F.-Y. Chen, Z.-Y. Wu, S. Gupta, D. J. Rivera, S. V. Lambeets, S. Pecaut, J. Y. T. Kim, P. Zhu, Y. Z. Finfrock, D. M. Meira, G. King, G. Gao, W. Xu, D. A. Cullen, H. Zhou, Y. Han, D. E. Perea, C. L. Muhich and H. Wang, *Nat. Nanotechnol.*, 2022, **17**, 759-767.

[33] Y. Sheng, R. Yang, K. Shi, H. Yu, K. Deng, Z. Wang, H. Wang, L. Wang and Y. Xu, *Chem. Eng. J.*, 2024, **485**, 149769.

[34] X. Chen, Y. Cheng, B. Zhang, J. Zhou and S. He, *Nat. Commun.*, 2024, **15**, 6278.

[35] W. He, J. Zhang, S. Dieckhöfer, S. Varhade, A. C. Brix, A. Lielpetere, S. Seisel, J. R. C. Junqueira and W. Schuhmann, *Nat. Commun.*, 2022, **13**, 1129.

[36] J. Yue, S. Liping, W. Yuechen, H. Lihua and Z. Hui, *Int. J. Hydrogen Energy*, 2024, **71**, 820-830.

[37] C. Xiao, Y. Guo, J. Sun, T. Guo, X. Jia, S. Guo, G. Wu, Y. Sun, Z. Yao and Y. Liu, *Nano Res.*, 2024, **17**, 5087-5094.

[38] W. Wen, P. Yan, W. Sun, Y. Zhou and X.-Y. Yu, *Adv. Funct. Mater.*, 2023, **33**, 2212236.

[39] J. Wang, C. Cai, Y. Wang, X. Yang, D. Wu, Y. Zhu, M. Li, M. Gu and M. Shao, *ACS Catal.*, 2021, **11**, 15135-15140.

[40] S. Zhang, J. Wu, M. Zheng, X. Jin, Z. Shen, Z. Li, Y. Wang, Q. Wang, X. Wang, H. Wei, J. Zhang, P. Wang, S. Zhang, L. Yu, L. Dong, Q. Zhu, H. Zhang and J. Lu, *Nat. Commun.*, 2023, **14**, 3634.

[41] J. Yang, H. Qi, A. Li, X. Liu, X. Yang, S. Zhang, Q. Zhao, Q. Jiang, Y. Su, L. Zhang, J.-F. Li, Z.-Q. Tian, W. Liu, A. Wang and T. Zhang, *J. Am. Chem. Soc.*, 2022, **144**, 12062-12071.

[42] W. Gao, K. Xie, J. Xie, X. Wang, H. Zhang, S. Chen, H. Wang, Z. Li and C. Li, *Adv. Mater.*, 2023, **35**, 2202952.

[43] K. Fan, W. Xie, J. Li, Y. Sun, P. Xu, Y. Tang, Z. Li and M. Shao, *Nat. Commun.*, 2022, **13**, 7958.